Centrifugal instability of stratified two-phase flow in a curved channel

Jason R. Picardo,[1] P. Garg,[2] and S. Pushpavanam[1,a]
[1]*Department of Chemical Engineering, Indian Institute of Technology Madras, Chennai 600 036, India*
[2]*Department of Chemical Engineering, Indian Institute of Technology Roorkee, Roorkee 247 667, India*

The centrifugal instability of stratified two-phase flow in a curved channel is investigated in this work. The fluids are laterally stratified between cylindrical walls of infinite extent. We focus on the limiting case of small capillary numbers (relatively high surface tension), wherein interfacial deformation and associated instabilities are suppressed. The centrifugal instability, caused by unstable gradients of angular momentum, destabilizes the axisymmetric azimuthal base flow. As in single phase Dean flow, an array of vortices is formed within each fluid at the critical Reynolds number. A numerical linear stability analysis is carried out using a recombined Chebyshev Galerkin spectral method, as well as a shooting method. Across the space of physical parameters (volume fractions, density, and viscosity ratios), six critical modes corresponding to distinct secondary flows are observed. These are classified into axisymmetric stationary vortices and rotating spiral vortices (travelling waves). Each category consists of three subtypes based on the relative vortex strength in the fluids: stronger in the outer fluid, stronger in the inner fluid, and comparable strength in both fluids. The critical mode switches amongst these six types as parameters are varied. The outer fluid is found to be more unstable than the inner fluid, even if the fluids have equal physical properties. This is explained using Rayleigh's criterion for inviscid flows. Consequently, the arrangement of fluids has a significant impact on stability. Instability and vortex motion are promoted if the fluid with a higher density, a lower viscosity, and a larger volume fraction is placed on the outer side of the channel. © *2015 AIP Publishing LLC.* [http://dx.doi.org/10.1063/1.4921631]

I. INTRODUCTION

Fluid flowing in a curved channel with infinitely tall walls has a unidirectional, fully developed base flow. However, centrifugal forces can destabilize this flow, as shown by Dean.[1] The no-slip condition at the outer wall causes angular momentum to decrease in the outward direction. This is an inherently unstable configuration. At a sufficiently high Reynolds number and curvature ratio (ratio of the channel's width to the radius of curvature of the inner wall), viscous forces are overcome and the base flow gives way to an array of axisymmetric vortices.[2,3] This *centrifugal instability* also arises in Taylor-Couette flow, in which fluid is driven by rotation of cylindrical walls.[2]

In this work, we analyze the impact of the centrifugal instability on two-phase Dean flow. The fluids are radially stratified between infinite concentric cylinders. The flow is pressure driven. The base flow is unidirectional and fully developed in the azimuthal direction (axisymmetric), with a cylindrical interface separating the fluids. We carry out a linear stability analysis to determine the

---

a)Author to whom correspondence should be addressed. Electronic mail: spush@iitm.ac.in. Telephone: +91-44-2254161. Fax: +91-44-22570509.

critical Reynolds number as a function of physical parameters and operating conditions. We also analyze features of the secondary flow arising at the onset of instability.

Investigations have been carried out on two-phase Taylor-Couette flow.[4,5] Recent work by Graham and coworkers[5–8] has been motivated by applications in liquid-liquid extraction. An important example is the separation of biological products from a carrier stream by contact with a solvent. Dispersing one fluid in another can damage biological molecules; hence, mass transfer across stratified fluids with a single interface is preferable. Onset of secondary circulations, due to the centrifugal instability, enhances mass transfer in these systems, while maintaining stratified flow. The two-phase pressure driven Dean flow considered here is a potential candidate for these applications.

A base state in which the fluids are radially stratified may be realized when centrifugal forces are strong enough to overcome gravitational forces and to prevent capillary breakup of the interface, due to interfacial tension forces. In two-phase Taylor-Couette flow, this is achieved by rotating the cylinders sufficiently rapidly. In the present two-phase Dean problem, the strength of centrifugal forces depends on the velocity of the pressure driven flow, which scales linearly with the pressure drop applied across the curved channel, $v_c = \frac{Gd^2}{\mu}$, where G is the pressure drop per unit length, d is the channel width, and μ is the mean viscosity of the fluids. Thus, centrifugal forces will dominate gravity when $\frac{v_c^2}{gR} \gg 1$ or $\frac{G^2 d^4}{\mu^2 gR} \gg 1$, where R is the radius of the inner wall. Graham and coworkers[5] found that capillary breakup of the cylindrical interface in Taylor-Couette flow is prevented when $\frac{(\rho_1 - \rho_2)(\Omega R_i)^2 R_i}{\gamma} \gg 1$, where Ω is the angular velocity of the cylinders, R_i is the location of the interface, and ρ_1 and ρ_2 are the densities of the inner and outer fluids, respectively. Analogously, we expect a stratified base state in two-phase Dean flow if $\frac{(\rho_1 - \rho_2)G^2 d^4 R_i}{\mu_1^2 \gamma} \gg 1$.

Previous work on two-phase Dean flow has been carried out by Gelfgat *et al.*[9] However, we find that their results significantly over predict the critical Reynolds number. An incomplete set of recombined Chebyshev functions was used as a basis in their Galerkin spectral method. Hence, the most dangerous modes were not described accurately. In this work, we adopt their basic Galerkin spectral technique but use a complete set of recombined Chebyshev functions as a basis for the two-fluid domain. The results of this method are cross-checked with a standard shooting technique.

While our focus in this work is on the centrifugal instability, the base flow is susceptible to other instabilities as well. These include *interfacial* and *non-interfacial* instabilities. In interfacial instabilities, deformation of the interface plays a key role and drives the secondary flow. The *Rayleigh-Taylor* instability[10] (due to centrifugal acceleration rather than gravitational), the *capillary* instability[11] (Rayleigh-Plateau), and the *viscosity-induced* instability are interfacial modes. The viscosity-induced mode is a result of the jump discontinuity in the radial gradient of the base velocity profile at the interface. This is caused by the balance of tangential shear stresses at the interface when the two fluids have different viscosities.[12,13] The category of non-interfacial modes includes the centrifugal instability and the *shear instability*. While the centrifugal instability is exclusively associated with curved channels, the shear instability occurs in straight channels as well[14,13] and is of the Tollmien-Schlichting type.[2] This instability occurs at a much higher value of the Reynolds number, compared to the other instability modes. In this classification, gravitational acceleration is neglected in comparison to centrifugal acceleration—an assumption which is maintained throughout this work.

To accurately interpret the results of a general linear stability analysis, in which all instabilities are significant, one must be able to distinguish these different instability modes. This requires a knowledge of their characteristic features, which can be obtained by studying simpler problems involving only a few modes. The literature contains detailed information on all these modes, except the two-phase centrifugal instability. Our aim, in this work, is to analyze the centrifugal mode in detail, under conditions when it dominates and is the primary source of instability.

Hence, we focus on the limit of small capillary numbers (*Ca*) (relatively strong surface tension forces). In this case, the viscosity-induced and Rayleigh-Taylor modes are suppressed by surface tension. The shear mode is unimportant since, in a curved channel, the centrifugal instability becomes unstable at much lower Reynolds numbers. (Gibson and Cook[15] have shown for single-phase
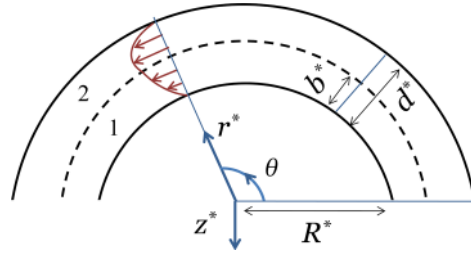
FIG. 1. Schematic of the flow system with a laterally stratified Poiseuille flow in a curved channel and the cylindrical coordinate system (r, z, θ). The positive z axis is perpendicular to the plane of the paper and extends outward.

flow that the curvature ratio must be smaller than 2.179×10^{-5} for the shear mode to be important at the onset of instability.) The capillary instability is also excluded if the curved walls of the channel have a radii of curvature larger than their height divided by 2π.[11] We shall assume this to be the case, with the understanding that the width of the channel is still sufficiently small compared to its height to allow its approximation by infinite cylinders. Thus, in the limit of small Ca, the centrifugal instability dominates the system.

The paper is organized as follows. The governing dynamic equations are presented in Sec. II and linearized about the base state in Sec. III. We then simplify the linear equations in the limit of small capillary numbers (Sec. IV). The resulting eigen value problem is solved in Sec. V. We begin our analysis in Sec. VI with a discussion of the mechanism of instability, along with Rayleigh's stability criterion. In Sec. VII, some important definitions of critical parameters are given. The different types of instability modes (from stationary toroidal vortices to rotating spirals) are presented and classified in Sec. VIII. We discuss the effect of the curvature ratio in Sec. IX before analyzing the effect of other parameters in Sec. X. Here, we pay close attention to transitions (mode switching) which occur between different types of instability modes as parameters are varied. In Sec. XI, we investigate the impact of interchanging the location of the two fluids on the system's stability. We conclude in Sec. XII, by summarizing the key results and discussing their significance.

II. GOVERNING DYNAMIC EQUATIONS

A schematic of the flow system is depicted in Figure 1, along with the cylindrical coordinate system (r, z, θ) adopted in the analysis. The z axis is perpendicular to the plane of the paper and extends to infinity.

The two fluids are radially stratified and the flow is driven by a pressure gradient imposed along the azimuthal direction. The base steady state (whose stability is to be determined) has a unidirectional, azimuthal flow. The velocity varies radially across the gap between the two cylinders. The inner and outer fluids are labelled 1 and 2, respectively. R^* is the radius of the inner cylinder, d^* is the gap width, and b^* is the width occupied by the inner fluid. The ratio of the gap width (d^*) to the radius of the inner cylinder (R^*) is the curvature ratio (a). $a = 0$ represents the case of parallel flat plates. The superscript (*) denotes dimensional quantities.

Governing dynamic equations (1a) and (1b) consist of the continuity equation and the Navier-Stokes equations, in cylindrical coordinates,

$$\nabla^* . \mathbf{v}_i^* = 0, \tag{1a}$$

$$\rho^* \left(\frac{\partial \mathbf{v}_i^*}{\partial t^*} + \mathbf{v}_i^* \cdot \nabla^* \mathbf{v}_i^* \right) = -\nabla^* \left(-G^* R^* \theta + p_i^* \right) + \mu^* \nabla^{2*} \mathbf{v}_i^*. \tag{1b}$$

Here, bold face symbols denote vectorial quantities. The subscript (i) takes the values 1 and 2 to denote the inner and outer fluids, respectively. $(-G^* R^*)$ is the constant azimuthal derivative of pressure which drives the unidirectional flow in the base state. All additional pressure variations are

contained in p_i^*. In the base state, p_i^* is independent of θ and z^* because the base flow is fully developed and invariant in z^*. It is however an increasing function of r^*, since the outward centrifugal force is balanced by the pressure distribution in the base state.

These equations are subject to the following boundary conditions in the radial direction. The no-slip condition at both lateral walls gives

$$\mathbf{v}_1^* = 0 \quad \text{at} \quad r^* = R^*, \tag{2}$$

$$\mathbf{v}_2^* = 0 \quad \text{at} \quad r^* = R^* + d^*. \tag{3}$$

Let the position of the interface be given by $r^* = H^*$, with $H^* = b^*$ in the base state. Then, the continuity of velocity at the interface implies

$$\mathbf{v}_1^* = \mathbf{v}_2^* \quad \text{at} \quad r^* = H^*. \tag{4}$$

The normal and tangential stress balances at the interface read

$$p_1^* - p_2^* + \left[\left(\tilde{\mathbf{n}} \cdot \tilde{\mathbf{n}} \cdot \mathbf{D}_2^* \right) - \left(\tilde{\mathbf{n}} \cdot \tilde{\mathbf{n}} \cdot \mathbf{D}_1^* \right) \right] = \gamma \left(\nabla \cdot \tilde{\mathbf{n}} \right) \quad \text{at} \quad r^* = H^*, \tag{5}$$

$$\tilde{\mathbf{n}} \cdot \mathbf{D}_2^* - \left(\tilde{\mathbf{n}} \cdot \tilde{\mathbf{n}} \cdot \mathbf{D}_2^* \right) \tilde{\mathbf{n}} = \tilde{\mathbf{n}} \cdot \mathbf{D}_1^* - \left(\tilde{\mathbf{n}} \cdot \tilde{\mathbf{n}} \cdot \mathbf{D}_1^* \right) \tilde{\mathbf{n}} \quad \text{at} \quad r^* = H^*. \tag{6}$$

Here, $\mathbf{D}_i^*$ is the deviatoric stress tensor and γ is the surface tension. $\tilde{\mathbf{n}}$ is the unit normal to the interface, directed into fluid 2. Denoting the unit vectors in the three coordinate directions as $\tilde{\mathbf{e}}_r, \tilde{\mathbf{e}}_z, \tilde{\mathbf{e}}_\theta$, we have

$$\tilde{\mathbf{n}} = \left(\tilde{\mathbf{e}}_r - \frac{\partial H^*}{\partial z^*} \tilde{\mathbf{e}}_z - \frac{1}{R^*} \frac{\partial H^*}{\partial \theta} \tilde{\mathbf{e}}_\theta \right) \left(1 + \left(\frac{\partial H^*}{\partial z^*} \right)^2 + \left(\frac{1}{R^*} \frac{\partial H^*}{\partial \theta} \right)^2 \right)^{-1/2}. \tag{7}$$

Finally, the kinematic condition must be satisfied at the interface,

$$\mathbf{v}_1 \cdot \left(\tilde{\mathbf{e}}_r - \frac{\partial H^*}{\partial z^*} \tilde{\mathbf{e}}_z - \frac{1}{R^*} \frac{\partial H^*}{\partial \theta} \tilde{\mathbf{e}}_\theta \right) = \frac{\partial H^*}{\partial t} \quad \text{at} \quad r^* = H^*. \tag{8}$$

Boundary effects in the z and θ directions are neglected in this stability analysis. The impact of this assumption on the form of perturbations assumed is discussed in Sec. III.

The pressure scale $(G^* d^*)$ and the gap width (d^*) are used to non-dimensionalize these equations. Since the base flow is stable when viscous forces dominate, we adopt a viscous scale for the velocity. Specifically, the velocity is scaled by $\frac{G^* d^{*2}}{12 \mu_1^*}$, which is the average velocity of fluid 1 when it flows in a unidirectional, fully developed manner between flat plates with a gap width of d^*. The dimensionless parameters which describe the system are the Reynolds number, capillary number, curvature ratio, position of the interface, ratios of viscosities, and densities of the two fluids,

$$Re = \frac{G^* d^{*3} \rho_1}{12 \mu_1^2}, \quad Ca = \frac{G^* d^{*2}}{12 \gamma}, \quad a = \frac{d^*}{R^*}, \quad b = \frac{b^*}{d^*}, \quad \mu_{12} = \frac{\mu_1}{\mu_2}, \quad \rho_{12} = \frac{\rho_1}{\rho_2}. \tag{9}$$

For convenience, the radial coordinate r^* is transformed to x, defined as $x = (r^* - R^*)/d^*$. The inner and outer walls of the curved channel correspond to $x = 0$ and $x = 1$, respectively.

To simplify the governing equations while retaining the essential physics, we make the *narrow gap* approximation or the *gentle curvature* approximation, which assumes that $d^* \ll R^*$ or $a \ll 1$. Effectively, this approximation eliminates the effect of curvature on the base flow but retains it in the linearized evolution equations; it is often used in the analysis of curved channel flows.[1,16] More detail on this assumption is provided in the online supplementary material.[17]

After transforming r^* to x, non-dimensionalizing and making the gentle curvature approximation, the governing equations reduce to the following:

$$\frac{\partial u_i}{\partial x} + a \frac{\partial v_i}{\partial \theta} + \frac{\partial w_i}{\partial z} = 0, \tag{10}$$

$$\frac{Re \mu_{1i}}{\rho_{1i}} \left[\frac{\partial u_i}{\partial t} + u_i \frac{\partial u_i}{\partial x} + a v_i \frac{\partial u_i}{\partial \theta} + w_i \frac{\partial u_i}{\partial z} - a v_i^2 \right] = -12 \mu_{1i} \frac{\partial p_i}{\partial x} + \frac{\partial^2 u_i}{\partial x^2} + a^2 \frac{\partial^2 u_i}{\partial \theta^2} + \frac{\partial^2 u_i}{\partial z^2}, \tag{11}$$

$$\frac{Re\mu_{1i}}{\rho_{1i}}\left[\frac{\partial w_i}{\partial t} + u_i\frac{\partial w_i}{\partial x} + av_i\frac{\partial w_i}{\partial \theta} + w_i\frac{\partial w_i}{\partial z}\right] = -12\mu_{1i}\frac{\partial p_i}{\partial z} + \frac{\partial^2 w_i}{\partial x^2} + a^2\frac{\partial^2 w_i}{\partial \theta^2} + \frac{\partial^2 w_i}{\partial z^2}, \quad (12)$$

$$\frac{Re\mu_{1i}}{\rho_{1i}}\left[\frac{\partial v_i}{\partial t} + u_i\frac{\partial v_i}{\partial x} + av_i\frac{\partial v_i}{\partial \theta} + w_i\frac{\partial v_i}{\partial z} + au_iv_i\right] = 12\mu_{1i} - 12a\mu_{1i}\frac{\partial p_i}{\partial \theta} + \frac{\partial^2 v_i}{\partial x^2} + a^2\frac{\partial^2 v_i}{\partial \theta^2} + \frac{\partial^2 v_i}{\partial z^2}.$$

$$(13)$$

Here, (u, w, v) are the non-dimensional velocities in the (x, z, θ) directions, respectively. Note that in spite of assuming a to be small, we have retained terms involving (aRe). This is because the flow becomes unstable as Re is increased, and its value can be quite large at the onset. We have also retained terms of the form $a\frac{\partial}{\partial \theta}$ and $a^2\frac{\partial^2}{\partial \theta^2}$ in order to account for short wavelength azimuthal disturbances.

III. LINEARIZATION

The base steady state consists of unidirectional fully developed (axisymmetric) flow in the azimuthal direction, i.e., $\bar{v}_i = V_i(x)\,\tilde{\mathbf{e}}_\theta$, where the azimuthal base velocity field is given by

$$V_1 = \frac{6x\left[b^2(1-\mu_{12}) + \mu_{12}\right]}{[b(1-\mu_{12}) + \mu_{12}]} - 6x^2, \tag{14a}$$

$$V_2 = \mu_{12}V_1 + \frac{6\mu_{12}b(1-b)(1-\mu_{12})}{[b(1-\mu_{12}) + \mu_{12}]}. \tag{14b}$$

Note that base flow profile (14) is a function of the interface position and the viscosity ratio alone and not of the Reynolds number or the density ratio. The pressure distribution in the base state is given by $-\frac{\theta}{a} + P_i(x)$, where $p_i = P_i(x)$ and may be determined from the momentum balance in the radial direction,

$$\frac{dP_i}{dx} = \frac{Re_i}{\rho_{1i}}\left(\frac{aV_i^2}{12}\right). \tag{15}$$

The governing Eqs. (10)–(13) are linearized about base states (14) and (15) by considering infinitesimally small perturbations to the base velocity and pressure fields,

$$u_i = \varepsilon\hat{u}_i(x)\exp\left[(kz + m\theta)i + \omega t\right], \tag{16a}$$

$$w_i = \varepsilon\hat{w}_i(x)\exp\left[(kz + m\theta)i + \omega t\right], \tag{16b}$$

$$v_i = V_i(x) + \varepsilon\hat{v}_i(x)\exp\left[(kz + m\theta)i + \omega t\right], \tag{16c}$$

$$p_i = P_i(x) + \varepsilon\hat{p}_i(x)\exp\left[(kz + m\theta)i + \omega t\right], \tag{16d}$$

$$H = b + \varepsilon h\exp\left[(kz + m\theta)i + \omega t\right]. \tag{16e}$$

Here, ε is the infinitesimal magnitude of the perturbations ($\varepsilon \ll 1$), which have typical normal mode forms. k and m are wave numbers in the z direction and the azimuthal direction, respectively. Since we focus on a temporal stability analysis, these wave numbers are restricted to real values while ω can be complex. Since the cylindrical walls extend to infinity in the z direction, the axial wave number is real, i.e., $k \in \mathbb{R}$.

In the azimuthal direction, boundary conditions must be imposed at the inlet and outlet of the curved channel. We have assumed periodic boundary conditions on the perturbations to facilitate a stability analysis using normal modes of the form $\exp\left[(kz + m\theta)i + \omega t\right]$. The permissible values of the azimuthal wave number m depend on the length of the curved channel. If the arc length of the inner wall is $\theta_L R^*$, then the azimuthal wave number m assumes a discrete set of real values given by $2\pi n/\theta_L$, with $n = 1, 2, 3, \ldots$. In order to study the maximum number of azimuthal modes, we consider the limiting case of $\theta_L = 2\pi$, which corresponds to $m = n = 1, 2, 3, \ldots$. In a practical curved channel, θ_L will be less than 2π, and some modes will be disallowed; e.g., if $\theta_L = \pi$, then $m = 2n = 2, 4, 6, \ldots$ and only even numbered modes are permitted.

The real part of ω (Re[ω]) is the growth rate; it describes the temporal growth/decay of the disturbance. The imaginary part of ω (Im[ω]) determines the temporal nature of the mode. If Im[ω] = 0, then the normal mode represents a stationary spatial wave, else it is a travelling wave which propagates in the direction $k\tilde{\mathbf{e}}_{\mathbf{z}} + m\tilde{\mathbf{e}}_{\boldsymbol{\theta}}$ with a phase speed of $-$Im[ω] $(k^2 + m^2)^{-1/2}$.

On substituting (16) into Eqs. (10)–(13) and linearizing (retaining terms of $O(\varepsilon^1)$), one obtains the following equations for the radial dependence of the perturbations ($\hat{u}_i, \hat{v}_i, \hat{w}_i, \hat{p}_i, h$):

$$\frac{d\hat{u}_i}{dx} + iam\hat{v}_i + ik\hat{w}_i = 0, \tag{17}$$

$$\frac{Re\mu_{1i}}{\rho_{1i}}\left(\omega\hat{u}_i + iamV_i\hat{u} - 2aV_i\hat{v}_i\right) = -12\mu_{1i}\frac{d\hat{p}_i}{dx} + \frac{d^2\hat{u}_i}{dx^2} - \left(a^2m^2 + k^2\right)\hat{u}_i, \tag{18}$$

$$\frac{Re\mu_{1i}}{\rho_{1i}}\left(\omega\hat{w}_i + iamV_i\hat{w}_i\right) = -12\mu_{1i}\left(ik\hat{p}_i\right) + \frac{d^2\hat{w}_i}{dx^2} - \left(a^2m^2 + k^2\right)\hat{w}_i, \tag{19}$$

$$\frac{Re\mu_{1i}}{\rho_{1i}}\left[\omega\hat{v}_i + \frac{\partial V_i}{\partial x}\hat{u}_i + iamV_i\hat{v}_i + aV_i\hat{u}_i\right] = -12\mu_{1i}\left(iam\hat{p}_i\right) + \frac{d^2\hat{v}_i}{dx^2} - \left(a^2m^2 + k^2\right)\hat{v}_i. \tag{20}$$

The boundary conditions for these equations are derived from (2) to (8), by linearizing and making the gentle curvature approximation. The interface boundary conditions, linearized by the method of domain perturbations,[11,18] are applied at $x = b$.

$$\hat{u}_1 = \hat{v}_1 = \hat{w}_1 = 0 \quad \text{at} \quad x = 0, \tag{21}$$

$$\hat{u}_2 = \hat{v}_2 = \hat{w}_2 = 0 \quad \text{at} \quad x = 1, \tag{22}$$

$$\hat{u}_1 = \hat{u}_2 \quad \text{at} \quad x = b, \tag{23}$$

$$\hat{w}_1 = \hat{w}_2 \quad \text{at} \quad x = b, \tag{24}$$

$$\hat{v}_1 + h\frac{dV_1}{dx} = \hat{v}_2 + h\frac{dV_2}{dx} \quad \text{at} \quad x = b, \tag{25}$$

$$12\left(\hat{p}_1 - \hat{p}_2\right) + 2\left(\frac{1}{\mu_{12}}\frac{d\hat{u}_2}{dx} - \frac{d\hat{u}_1}{dx}\right) = \frac{1}{Ca}\left(-a^2 + k^2 + a^2m^2\right)h \quad \text{at} \quad x = b, \tag{26}$$

$$\mu_{12}\left(ik\hat{u}_1 + \frac{d\hat{w}_1}{dx}\right) = \left(ik\hat{u}_2 + \frac{d\hat{w}_2}{dx}\right) \quad \text{at} \quad x = b, \tag{27}$$

$$\mu_{12}\left(\frac{d\hat{v}_1}{dx} + ima\hat{u}_1\right) = \frac{d\hat{v}_2}{dx} + ima\hat{u}_2 \quad \text{at} \quad x = b, \tag{28}$$

$$\hat{u}_1 - imaV_1h = \omega h \quad \text{at} \quad x = b. \tag{29}$$

Equations (17)–(29) constitute an eigenvalue problem in which (ω) is the complex eigenvalue. On solving this eigenvalue problem for a specified disturbance mode (defined by the wave numbers k and m) and fixed parameter values, a spectrum of complex eigenvalues is obtained. The entire spectrum must be in the left half of the complex plane (Re[ω] $\leq$ 0) for the system to be stable to the disturbance. The onset of instability occurs when the real part of one or more eigenvalues first becomes zero. The modes corresponding to these critical eigenvalues are called critical modes; they determine the nature of the secondary flow close to the onset of instability.[19]

IV. LIMIT OF SMALL CAPILLARY NUMBER

In this work, we consider the limit of small capillary numbers ($Ca \ll 1$), for which interfacial deformation does not impact the onset of instability or the secondary flow significantly. To derive simplified equations for this limit, we expand the eigenfunctions $\hat{u}_i, \hat{v}_i, \hat{w}_i, \hat{p}_i, h$ as power series in Ca as follows:

$$\{\hat{u}_i, \hat{v}_i, \hat{w}_i, \hat{p}_i\} = \{\hat{u}_{i,0}, \hat{v}_{i,0}, \hat{w}_{i,0}, \hat{p}_{i,0}\} + \{\hat{u}_{i,1}, \hat{v}_{i,1}, \hat{w}_{i,1}, \hat{p}_{i,1}\}Ca + O\left(Ca^2\right), \tag{30}$$

$$h = h_0 + h_1Ca + O\left(Ca^2\right). \tag{31}$$

Substituting these expansions into (17)–(29) and equating coefficients of like powers of Ca, we obtain a sequence of linear equations for every order of the expansion. The domain equations remain unchanged, as they do not contain Ca. The boundary conditions however are simplified. At $O(Ca^0)$, normal stress condition (26) reduces to

$$(-a^2 + k^2 + a^2 m^2) h_0 = 0. \tag{32}$$

This equation implies that the interface is undeformed at $O(Ca^0)$, $h_0 = 0$, unless the prefactor $(-a^2 + k^2 + a^2 m^2)$ is zero. The latter case occurs only when the disturbance is axisymmetric ($m = 0$) and if $k = a$. This condition on k corresponds to the cutoff axial wave number for capillary instability; a curved interface is unstable to capillary breakup when $k < a$, or the axial wavelength $(2\pi d^*/k)$ is greater than the circumference of the circular interface ($\approx 2\pi R^*$). The coefficients in the series expansion of h (31) can be determined only if $k \neq a$. This is guaranteed if the height of the cylindrical walls (L) is less than the circumference of the inner cylinder ($2\pi R^*$), i.e., if $k > a$. This condition effectively stabilizes the system to capillary instability[11] and ensures that interfacial deformations are negligibly small as Ca approaches zero. Note that even with this restriction on the height of the walls (L), we may approximate them as semi-infinite cylinders provided $d^* \ll L < R^*$. Under these conditions, the prefactor $(-a^2 + k^2 + a^2 m^2)$ is nonzero and positive and (32) yields $h_0 = 0$.

Thus for small capillary numbers, the stability threshold of the system and the critical eigen modes can be approximated by analyzing the problem with a non-deforming interface. The simplified boundary conditions at $O(Ca^0)$ are

$$\hat{u}_{1,0} = \hat{v}_{1,0} = \hat{w}_{1,0} = 0 \quad \text{at} \quad x = 0, \tag{33}$$

$$\hat{u}_{2,0} = \hat{v}_{2,0} = \hat{w}_{2,0} = 0 \quad \text{at} \quad x = 1, \tag{34}$$

$$\hat{u}_{1,0} = \hat{u}_{2,0} \quad \text{at} \quad x = b, \tag{35}$$

$$\hat{w}_{1,0} = \hat{w}_{2,0} \quad \text{at} \quad x = b, \tag{36}$$

$$\hat{v}_{1,0} = \hat{v}_{2,0} \quad \text{at} \quad x = b, \tag{37}$$

$$\mu_{12} \left(ik\hat{u}_{1,0} + \frac{d\hat{w}_{1,0}}{dx} \right) = \left(ik\hat{u}_{2,0} + \frac{d\hat{w}_{2,0}}{dx} \right) \quad \text{at} \quad x = b, \tag{38}$$

$$\mu_{12} \left(\frac{d\hat{v}_{1,0}}{dx} + ima\hat{u}_{1,0} \right) = \frac{d\hat{v}_{2,0}}{dx} + ima\hat{u}_{2,0} \quad \text{at} \quad x = b, \tag{39}$$

$$\hat{u}_{1,0} = 0 \quad \text{at} \quad x = b. \tag{40}$$

These boundary conditions along with the domain equations at $O(Ca^0)$, derived from (17) to (20), specify the eigen value problem for $\hat{u}_{i,0}, \hat{v}_{i,0}, \hat{w}_{i,0}, \hat{p}_{i,0}$.

In this work, we do not proceed to calculate the corrections to the eigenfunction and growth rate at higher orders in Ca. However, the first approximation to the small deformations of the interface can be calculated, without extra effort, from normal stress condition (26) at $O(Ca)$,

$$h_1 = \frac{1}{(-a^2 + k^2 + a^2 m^2)} \left[12 (\hat{p}_{1,0} - \hat{p}_{2,0}) + 2 \left(\frac{1}{\mu_{12}} \frac{d\hat{u}_{2,0}}{dx} - \frac{d\hat{u}_{1,0}}{dx} \right) \right] \quad \text{at} \quad x = b. \tag{41}$$

Since $\hat{u}_{i,0}$ and $\hat{p}_{i,0}$ are known from the solution of the zeroth order problem, (41) provides an explicit formula for evaluating h_1—the deformation of the interface at $O(Ca)$.

Note that considering the limit of small Ca, when Re is fixed, is equivalent to considering the limit of small Weber number (We) because $We = ReCa$.

V. SOLUTION OF THE EIGENVALUE PROBLEM

In this section, we solve the eigenvalue problem to $O(Ca^0)$ by applying two numerical schemes—a novel two-phase recombined Chebyshev Galerkin spectral (RCGS) method and a standard shooting method. First, the domain equations (17)–(20) are simplified by eliminating $\hat{p}_{i,0}$ using (19) and $\hat{w}_{i,0}$ using (17). These manipulations result in a fourth order equation for $\hat{u}_{i,0}$ and a second

order equation for $\hat{v}_{i,0}$,

$$
\begin{aligned}
\omega & \left[\frac{Re_i \mu_{1i}}{\rho_{1i}} \frac{(a^2m^2 + k^2)}{k^2} \hat{u}_{i,0} - \frac{Re_i \mu_{1i}}{\rho_{1i}} \frac{1}{k^2} \frac{d^2\hat{u}_{i,0}}{dx^2} \right] = -\frac{1}{k^2} \frac{d^4\hat{u}_{i,0}}{dx^4} \\
& + \left(2\frac{(a^2m^2 + k^2)}{k^2} + \frac{Re_i \mu_{1i}}{\rho_{1i}} \frac{am}{k^2} V_i i \right) \frac{d^2\hat{u}_{i,0}}{dx^2} - \frac{Re_i \mu_{1i}}{\rho_{1i}} \left(\frac{a^2m}{k^2} V_i i \right) \frac{d\hat{u}_{i,0}}{dx} \\
& - \left(\frac{(a^2m^2 + k^2)^2}{k^2} + \frac{Re_i \mu_{1i}}{\rho_{1i}} \frac{am(a^2m^2 + k^2)}{k^2} V_i i + \frac{Re_i \mu_{1i}}{\rho_{1i}} \frac{am}{k^2} \left(\frac{d^2V_i}{dx^2} + a\frac{dV_i}{dx} \right) i \right) \hat{u}_{i,0} \\
& + \left(\frac{Re_i \mu_{1i}}{\rho_{1i}} \frac{2aV_i(a^2m^2 + k^2)}{k^2} \right) \hat{v}_{i,0},
\end{aligned}
\tag{42}
$$

$$
\begin{aligned}
\omega & \left[-\frac{Re_i \mu_{1i}}{\rho_{1i}} \left(\frac{am}{k^2} i \right) \frac{d\hat{u}_{i,0}}{dx} + \frac{Re_i \mu_{1i}}{\rho_{1i}} \left(1 + \frac{a^2m^2}{k^2} \right) \hat{v}_{i,0} \right] = -\left(\frac{am}{k^2} i \right) \frac{d^3\hat{u}_{i,0}}{dx^3} \\
& + \left(\frac{am}{k^2} (a^2m^2 + k^2) i - \frac{Re_i \mu_{1i}}{\rho_{1i}} \frac{a^2m^2}{k^2} V_i \right) \frac{d\hat{u}_{i,0}}{dx} - \frac{Re_i \mu_{1i}}{\rho_{1i}} \left(\frac{dV_i}{dx} + aV_i \right) \hat{u}_{i,0} \\
& + \left(1 + \frac{a^2m^2}{k^2} \right) \frac{d^2\hat{v}_{i,0}}{dx^2} - \left(\frac{(a^2m^2 + k^2)^2}{k^2} + \frac{Re_i \mu_{1i}}{\rho_{1i}} amV_i \frac{(a^2m^2 + k^2)}{k^2} i \right) \hat{v}_{i,0}.
\end{aligned}
\tag{43}
$$

The boundary conditions for (42) and (43) are obtained from (33) to (40),

$$
\hat{u}_{1,0} = \frac{d\hat{u}_{1,0}}{dx} = 0 \quad \text{at} \quad x = 0,
\tag{44}
$$

$$
\hat{u}_{2,0} = \frac{d\hat{u}_{2,0}}{dx} = 0 \quad \text{at} \quad x = 1,
\tag{45}
$$

$$
\hat{u}_{1,0} = \hat{u}_{2,0} = 0 \quad \text{at} \quad x = b,
\tag{46}
$$

$$
\frac{d\hat{u}_{1,0}}{dx} = \frac{d\hat{u}_{2,0}}{dx} \quad \text{at} \quad x = b,
\tag{47}
$$

$$
\mu_{12} \frac{d^2\hat{u}_{1,0}}{dx^2} = \frac{d^2\hat{u}_{2,0}}{dx^2} \quad \text{at} \quad x = b,
\tag{48}
$$

$$
\hat{v}_{1,0} = 0 \quad \text{at} \quad x = 0,
\tag{49}
$$

$$
\hat{v}_{2,0} = 0 \quad \text{at} \quad x = 1,
\tag{50}
$$

$$
\hat{v}_{1,0} = \hat{v}_{2,0} \quad \text{at} \quad x = b,
\tag{51}
$$

$$
\mu_{12} \frac{d\hat{v}_{1,0}}{dx} = \frac{d\hat{v}_{2,0}}{dx} \quad \text{at} \quad x = b.
\tag{52}
$$

Here, the conditions on the first derivative of $\hat{u}_{i,0}$ are derived from the boundary conditions on $\hat{w}_{i,0}$.

This eigenvalue problem, (42)–(52), is solved numerically, as described in Subsections V A and V B.

A. Two-phase RCGS method

In this method, a set of basis functions which analytically satisfy all the boundary conditions of the eigen value problem is constructed from combinations of Chebyshev functions. Using this "recombined" basis set, the Galerkin procedure is applied to obtain a matrix eigen value problem which is readily solved by QZ decomposition. While this conceptual framework has been in place for several years, it is only with the recent and rapid increase of computer memory that it has become a viable numerical strategy. This has coincided with the development of symbolic computing packages, such as Mathematica, which may be used to construct the basis set easily and implement the entire procedure efficiently. The revival of this method is largely due to Gelfgat and coworkers, who have successfully applied it to single-phase problems.[20–22]

The two-phase RCGS method is explained in detail in the supplementary material.[17] Here, we outline the procedure in brief. The functions $\hat{u}_{1,0}$ and $\hat{u}_{2,0}$ defined on $[0, b]$ and $[b, 1]$, respectively, are combined into a single vector function $\hat{\mathbf{u}}_{\mathbf{0}} = (\hat{u}_{1,0}, \hat{u}_{2,0})^{\mathrm{T}}$ defined over the entire domain $[0, 1]$. Similarly, we define $\hat{\mathbf{v}}_{\mathbf{0}} = (\hat{v}_{1,0}, \hat{v}_{2,0})^{\mathrm{T}}$. Here, the superscript T denotes the transpose operation. $\hat{\mathbf{u}}_{\mathbf{0}}$ and $\hat{\mathbf{v}}_{\mathbf{0}}$ belong to the direct sum Hilbert space $\mathcal{L}_2[0, b] \oplus \mathcal{L}_2[b, 1]$. These combined functions are expanded in terms of basis sets $\{\boldsymbol{\varphi}_{\mathbf{u}, n}\}_{n=0}^{\infty}$ and $\{\boldsymbol{\varphi}_{\mathbf{v}, n}\}_{n=0}^{\infty}$, respectively,

$$\hat{\mathbf{u}}_{\mathbf{0}} = \sum_{n=0}^{N} c_n \boldsymbol{\varphi}_{\mathbf{u}, n} \quad \text{and} \quad \hat{\mathbf{v}}_{\mathbf{0}} = \sum_{n=0}^{N} d_n \boldsymbol{\varphi}_{\mathbf{v}, n}. \tag{53}$$

Each $\boldsymbol{\varphi}_{\mathbf{u}, n}$ satisfies the boundary conditions on $\hat{u}_{1,0}$ and $\hat{u}_{2,0}$ ((44)–(48)), while each $\{\boldsymbol{\varphi}_{\mathbf{v}, n}\}_{n=0}^{\infty}$ satisfies the boundary conditions on $\hat{v}_{1,0}$ and $\hat{v}_{2,0}$ ((49)–(52)). The construction of these basis functions is described in the supplementary material.[17]

The Galerkin procedure is then applied to discretize (42) and (43). The inner products are evaluated using Gaussian quadrature (cf. supplementary material[17]). This results in a generalized matrix eigenvalue problem,

$$\mathbf{A}\mathbf{x} = \omega \mathbf{B}\mathbf{x}, \tag{54}$$

where $\mathbf{x}$ is the vector of $2(N+1)$ unknown coefficients, $\{c_n\}_{n=0}^{N} \cup \{d_n\}_{n=0}^{N}$. $\mathbf{A}$ and $\mathbf{B}$ are square, *non-singular* matrices of dimension $2(N+1) \times 2(N+1)$. Non-singularity of $\mathbf{B}$ is a particular advantage of the two-phase RCGS method over traditional collocation or Tau spectral methods.

Matrix eigenvalue problem (54) is solved by QZ-decomposition (zgeev routine of LAPACK) to yield a set of $2(N+1)$ eigenvalues which approximates the point spectrum of differential eigenvalue problem (42)–(52). For some parameter values, a single positive spurious eigenvalue is obtained from the computation. It is typically two orders of magnitude greater than the true eigenvalues and thus can be easily identified and eliminated.

Results of the RCGS method are cross-checked with those obtained using a shooting method with orthonormalization. The shooting technique is described in Subsection V B. The two methods are in good agreement, as demonstrated by the example presented in the supplementary material.[17] Numerical results demonstrating the convergence characteristics of the two-phase RCGS method are also presented in the supplementary material.[17] Twenty four basis functions are found to provide sufficient accuracy for all the cases considered in this work.

B. Shooting method with orthonormalization

We also use a shooting method with orthonormalization to solve (42)–(52). This method is based on a technique described by Conte.[23] A similar approach has been used successfully to solve the single phase Orr-Sommerfeld equations[24,2] and to study the stability of two-phase stratified plane Poiseuille flow.[25] This method is fundamentally different from the spectral method discussed in Sec. V A. It is an iterative local method which, rather than approximating the entire spectrum, allows the determination of a single eigenvalue starting from an initial guess. Alternatively, the marginal Reynolds number, which marks the stability boundary, can be directly identified by setting the growth rate to zero ($\text{Re}[\omega] = 0$) and treating the Reynolds number as an eigen value. The smallest value of the Reynolds number obtained from the shooting method is the marginal Reynolds number.

VI. RAYLEIGH'S INVISCID STABILITY CRITERION

The centrifugal instability is caused by an unstable stratification of angular momentum in any one (or both) of the fluids. If the angular momentum of the base flow, $xV_i(x)$, decreases radially outward, then centrifugal forces have a tendency to induce circulations and destabilize the flow.[2] This situation is analogous to the case of a density stratified fluid at rest in a gravitational field. If the density decreases in the direction of the gravitational force, then the stationary state is unstable.

For the case of single-phase inviscid flow in a curved channel, Rayleigh's criterion gives a formal stability condition.[2] It is valid for axisymmetric disturbances. This single phase result may
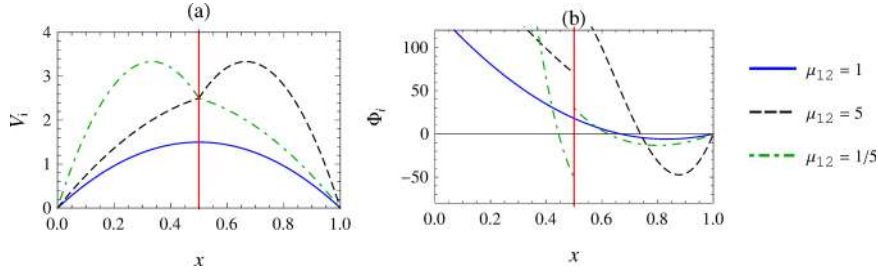
FIG. 2. Plots of the base velocity profile for different viscosity ratios and the corresponding profiles of the Rayleigh discriminant $\Phi_i(x)$. In the plot for $\mu_{12} = 1/5$, the velocity has been rescaled with μ_2 (rather than μ_1, as is done throughout this work) to facilitate a clear comparison with the plot for $\mu_{12} = 5$.

be directly extended to the case of stratified inviscid fluids, if the regime of small Ca is considered, wherein interfacial deformation is negligible. Here, Rayleigh's criterion may be applied separately to each fluid, since the linear stability equations for the two fluids are independent and individually identical to the single-phase equations. The criterion is based on the value of the Rayleigh discriminant in each fluid $\Phi_i(x)$ given below,

$$\Phi_i(x) = \frac{1}{x^3} \frac{d}{dx}(xV_i(x))^2. \tag{55}$$

If $\Phi_i(x) < 0$ within the domain of either fluid, then the inviscid base flow is unstable. In the case of viscous fluids, the flow is stabilized by viscous dampening at low Reynolds number. However, when the Reynolds number exceeds a critical value, the centrifugal instability will set in.

In Figure 2, base velocity profiles (14) and the corresponding values of the Rayleigh discriminant are plotted for different viscosity ratios. $\Phi_i(x)$ varies considerably across the channel and is discontinuous at the interface when the fluids have different viscosities. (This is induced by the balance of tangential stresses, cf. (6).) Figure 2 shows that $\Phi_i(x)$ is generally positive near the inner wall and negative near the outer wall. This is because the velocity is zero at both walls (no-slip condition); as we move from the inner to the outer wall, the velocity first increases, attains a maximum, and then decreases again. $\Phi_i(x)$ can also be negative in the inner fluid, if the maximum is located within the inner fluid. This occurs when $\mu_{12} < 1$ (e.g., $\mu_{12} = 1/5$ in Figure 2) or $b > 0.5$. In all cases, since $\Phi_i(x) < 0$ in some part of the flow, the centrifugal instability will destabilize the base state, beyond a critical Reynolds number.

The regions where $\Phi_i(x) < 0$ are said to be *locally unstable* while the regions of positive $\Phi_i(x)$ are termed *locally stable*. In single-phase flow, it has been shown that the magnitude of the secondary flow at the onset of instability is greater within the locally unstable regions.[2,16] Extending this to two-phase flows, one can expect a stronger secondary flow within the fluid with a more negative value of $\Phi_i(x)$. This has been confirmed for two-phase *Taylor-Couette* flow.[5] Based on Figure 2, we expect a stronger secondary flow within the outer fluid for a majority of parameter values. Physically, this implies that the outer fluid has a more unstable stratification of angular momentum, even if the fluids have similar properties.

VII. DEFINITION OF MARGINAL AND CRITICAL REYNOLDS NUMBERS

We now define some key stability parameters which are used in the presentation of results. For a specified disturbance mode (fixed values of k and m) and fixed values of physical parameters, the Reynolds number at which the maximum of Re[ω] (growth rate) is zero is defined as the *marginal Reynolds number* (Re_{mg}). The system is unstable to the specified disturbance for all Reynolds numbers greater than Re_{mg}. Clearly, the marginal Reynolds number is a function of the disturbance (k and m).

In Figure 3, the marginal Reynolds number is plotted for different disturbance modes, for the case of $\mu_{12} = 0.5$, $\rho_{12} = 0.5$, $b = 0.5$, and $a = 0.1$. These are the neutral stability curves. For a given
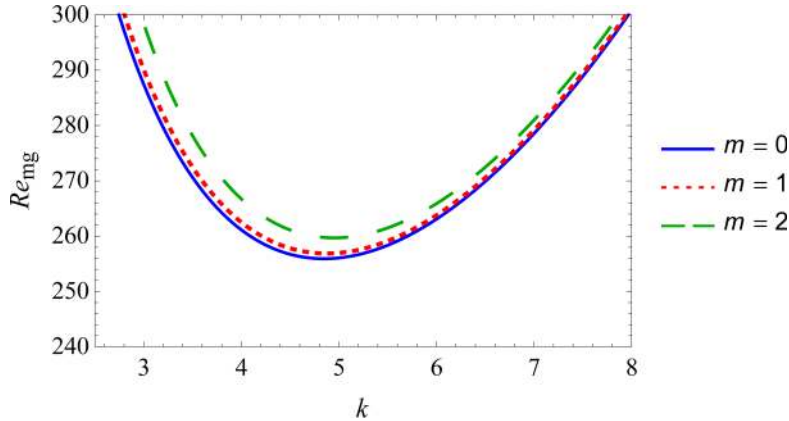
FIG. 3. Marginal Reynolds number (Re_{mg}) for various disturbance modes. The minima of each curve corresponds to the least marginal Reynolds number ($Re_{c,m}$) at each value of m. These are $Re_{c,m} = 255.92$, $k_{c,m} = 4.85$ ($m = 0$); $Re_{c,m} = 256.87$, $k_{c,m} = 4.88$ ($m = 1$); and $Re_{c,m} = 259.69$, $k_{c,m} = 4.95$ ($m = 2$). The critical mode in this case is $m_c = 0$, $k_c = 4.85$, and $Re_c = 255.92$, which is axisymmetric. Parameter values: $\mu_{12} = 0.5$, $\rho_{12} = 0.5$, $b = 0.5$, and $a = 0.1$.

azimuthal wave number (m), the smallest value of Re_{mg} across all k is called the *least marginal Reynolds number* and denoted by $Re_{c,m}$. The corresponding axial wave number is $k_{c,m}$.

In Figure 3, the smallest value of $Re_{c,m}$ corresponds to the axisymmetric mode, $m = 0$ (details are given in the figure caption). This is called the *critical Reynolds number Re_c* and the corresponding disturbance mode is the *critical instability mode* (k_c, m_c). In Figure 3, we have $m_c = 0$, $k_c = 4.85$, and $Re_c = 255.92$. Centrifugal instability first occurs when Re exceeds Re_c.

Neutral stability curves of qualitative structure similar to those in Figure 3 occur for a variety of physical problems. Well known examples are the Rayleigh-Benard instability and Turing patterns.[19] These instabilities, classified as type-I by Cross and Hohenberg, exhibit similar linear stability characteristics and weakly nonlinear behavior.[26]

VIII. CLASSIFICATION OF INSTABILITY MODES

Just above the critical point, when the Reynolds number slightly exceeds Re_c, only modes in a close neighborhood of k_c, m_c will be unstable (cf. Figure 3). After an initial period of exponential growth, the ensuing three dimensional flow will saturate via nonlinear mechanisms to a new flow state. The spatiotemporal variation of the new flow will correspond closely to the critical mode $\hat{\mathbf{v}}_{i,0}(x) \exp(ikz + im\theta + i\omega t)$ (assuming a supercritical bifurcation), provided Re is sufficiently close to Re_c.[19] Thus, a significant change in the nature of the critical mode signifies a new type of secondary flow pattern.

The critical instability mode and the corresponding secondary flow state can be of two types, depending on the value of $\text{Im}[\omega]$ at the critical point (when $\text{Re}[\omega] = 0$). If $\text{Im}[\omega] = 0$, then the instability is stationary and the new emergent state is a steady state. On the other hand if $\text{Im}[\omega]$ is non-zero, the instability is oscillatory. Such a mode can take the form of either a travelling or standing wave. Standing waves are ruled out in this problem due to the absence of reflection symmetry in the azimuthal direction (because of the base flow). Hence, when $\text{Im}[\omega]$ is nonzero, the critical mode is a travelling wave.

This temporal nature of the instability is closely connected to the azimuthal dependence of the critical mode. Linearized equations (42) and (43) reveal that *an axisymmetric critical mode is stationary while a non-axisymmetric mode is a travelling wave*. If the mode is axisymmetric ($m_c = 0$) then the simplified eigenvalue problem is real and we find that $\text{Im}[\omega] = 0$ for the critical mode. On the other hand if m_c is non-zero, then eigenvalue problem (42) and (43) is complex and $\text{Im}[\omega]$ is non-zero.
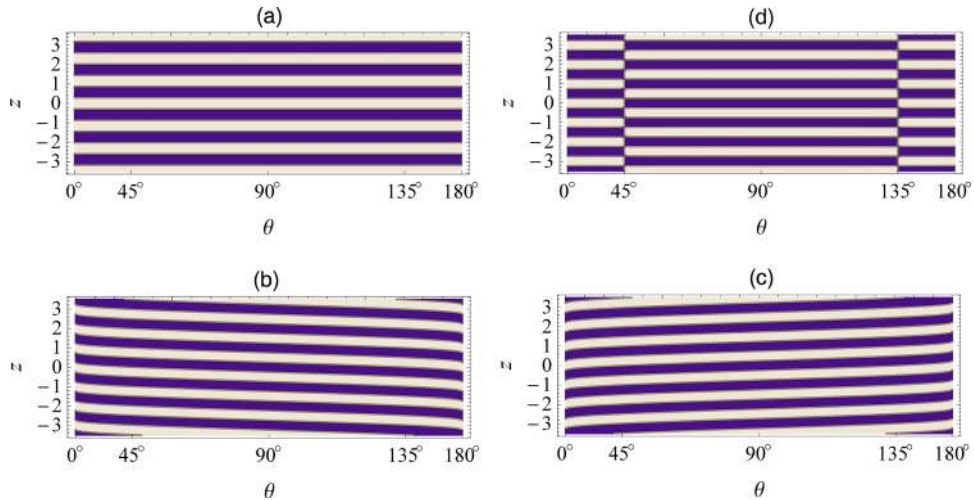
FIG. 4. Visualization of different vortex array patterns (external structure) corresponding to critical modes at different parameter values. (a) axisymmetric toroidal vortices, (b) left handed rotating spirals, (c) right handed rotating spirals, and (d) ribbon vortex state-superposition of (b) and (c). The dark and light regions correspond to different vortex regions across which the fluid does not mix. Each figure represents the external structure of a critical mode as seen through the outer cylindrical wall. Hence, linear positions along the x axis correspond to $R^* \cos(\theta)/a^*$. A visualization window with a small axial length is selected for better clarity, and the axes in the figures are drawn to scale for a more realistic visualization. Parameter values: (a) $Re_c = 36.049$, $k_c = 5.43$, $m_c = 0$, $Im[\omega_c] = 0$, $\mu_{12} = 1.9$, $\rho_{12} = 0.5$, $b = 0.5$; (b) $Re_c = 391.378$, $k_c = 6.32$, $m_c = 2$, $Im[\omega_c] = -0.227$, $\mu_{12} = 0.66$, $\rho_{12} = 0.3$, $b = 0.76$; and (c) $Re_c = 391.378$, $k_c = -6.32$, $m_c = 2$, $Im[\omega_c] = -0.227$, $\mu_{12} = 0.66$, $\rho_{12} = 0.3$, $b = 0.76$. In all cases, $a = 0.1$. (Multimedia view) [URL: http://dx.doi.org/10.1063/1.4921631.1]

A. Stationary axisymmetric vortices and rotating spirals

We discuss the temporal nature of the modes along with their azimuthal dependence, as these are interconnected. In Figure 4, we plot the variation along the z-θ surface of two modes with distinct spatio-temporal behavior. These plots depict the vortex arrays as seen through the surface of the outer cylindrical wall. Each plot corresponds to a critical mode computed for specific parameter values which are given in the caption. The temporal nature of these vortex patterns is depicted in the accompanying movie (cf. Figure 4) (Multimedia view).

Figure 4(a) corresponds to an axisymmetric and stationary critical mode which manifests as toroidal vortices. These vortices are two-phase analogues of single phase Dean vortices.[16] Similar axisymmetric vortices have been observed experimentally in two-phase Taylor-Couette flow (cf. Fig. 11 in Ref. 5).

Figures 4(b) and 4(c) depict two non-axisymmetric travelling modes. These modes have identical mathematical descriptions, except for the sign of k_c. Both modes become critical simultaneously, as eigenvalue problem (42)–(52) is invariant to the sign of k_c. They have the structure of spirals which start at the inlet of the channel and terminate at the outlet. They appear to rotate and propagate through the cylinder. The case in Figure 4(b) corresponds to $k_c > 0$. This is a left-handed spiral which propagates axially upward. The other mode, in Figure 4(c), has $k_c < 0$ and is a right handed spiral that propagates axially downward. In fact, these two modes are reflections of each other about the r-θ plane. We expect the spiral flow pattern that emerges when a non-axisymmetric mode is critical to be distorted at the inlet and outlet of the channel due to boundary effects. However, away from these boundaries, the non-axisymmetric critical modes are expected to manifest clearly as rotating spiral vortices.

The simultaneous criticality of both types of spiral modes is a natural outcome of symmetry-breaking.[27,28] The base flow possesses reflection symmetry in the z direction. While the axisymmetric stationary modes retain this symmetry, the spiral travelling waves break it. When reflection symmetry is broken at the onset of instability, the set of possible emerging flow states should be related to each other via the same reflection transformation, i.e., reflection of any one spiral state

about the r-θ plane should yield another equally possible spiral flow state. Depending on the initial perturbation, either mode can dominate and lead to a left or right-handed rotating spiral flow.

These degenerate spiral modes can also superpose with equal amplitudes and give rise to a new state which only propagates azimuthally. This combined mode is depicted in Figure 4(d) and is called a ribbon state.[29] The ribbon flow is a standing wave with respect to the axial direction. It is known that for type-I instabilities (which includes the centrifugal instability), if both travelling waves and standing waves are critical (according to the linear theory) then only one of the two can be stable.[26,19] The stability is parameter dependent and may be determined from the associated amplitude equations. Hence for parameter values which support rotating spirals, the ribbon state will not be observed and vice versa. Both patterns have been observed experimentally in Taylor-Couette flow.[30] It should be noted that in the single-phase Dean problem, the axisymmetric mode is always critical and hence, only axisymmetric stationary vortices like those in Figure 4(a) have been reported. On the other hand, the two-phase problem has a higher degree of freedom. It involves many more parameters which affect the inter-fluid interaction giving rise to spirals or ribbon flow states.

B. Internal circulatory flow structure

Having described the external vortex pattern of the critical modes (z, θ variation), we now turn to their internal flow structure (x or radial variation). We find three distinct types, based on the relative strength of the circulatory flow within the two fluids: (i) the inner fluid circulates faster, (ii) the outer fluid circulates faster, and (iii) both fluids have comparable cross flow velocities. This difference of the secondary flow within the two fluids originates from the stratification of angular momentum in the base flow. The profile of the Rayleigh discriminant (cf. Sec. VI) is indicative of this dissimilarity between the fluids.

The first two cases of the internal vortex structures are illustrated for axisymmetric modes in Figure 5. Here, the eigenfunctions have been normalized such that the coefficient of $\boldsymbol{\varphi_{u,1}}$ is unity. The magnitude of the circulatory flow in the two fluids may be compared using the line plot of the z-component of velocity along the centreline of the vortices in the upper half of the axial periodic cell, i.e., $z = \pi/(4k_c)$. Figure 5(a) is an example of a mode with stronger circulatory flow in the outer fluid. Such modes are called *outer* modes. Figure 5(b) exemplifies the opposite scenario; it is called an *inner* mode. Based on k_c, we observe that the vortices are generally larger (k_c is smaller) in the outer mode (compare the scales of the z axes in Figures 5(a) and 5(b)). A similar disparity in the magnitude of circulatory flow within the two fluids has been observed in critical modes of two-phase Taylor-Couette flow.[5]

The third case, wherein the secondary flow is of comparable magnitude in both fluids, is called a *uniform* mode. An example is presented in Figure 6. This particular critical two-phase mode is also present in single phase Dean flow, as an experimentally unobservable mode. Single phase flow bifurcates to Dean vortices at $Re_c = 121.35$ ($a = 0.1$). On increasing the Reynolds number beyond critical, we find that a second eigenvalue crosses the imaginary axis at $Re = 593.92$. The corresponding eigenfunction is the second most unstable single phase mode. This mode has exactly the same structure as the uniform two phase mode shown in Figure 6.

C. Six categories of instability modes

Altogether we have identified six different types of critical modes, based on their temporal nature and vortex pattern. We assign the letter S for stationary axisymmetric modes and the letter T for travelling spiral modes. The radial vortex structure of these modes can correspond to either outer, inner, or uniform modes, which we denote by the letters O, I, and U, respectively. Thus, we have six different classes of critical modes, labelled as O-S, O-T, I-S, I-T, U-S, and U-T. The nature of the critical mode can change from one type to another as the parameters are varied. Examples of such transitions are presented in Sec. X, along with a discussion of physical causes for mode switching.
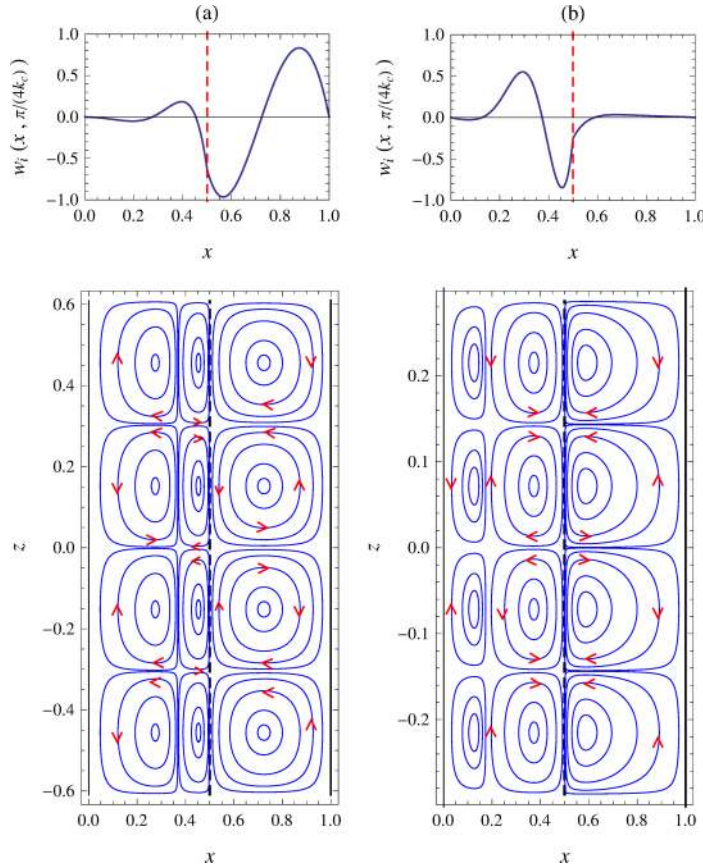
FIG. 5. Internal circulatory flow structure of the critical modes at the onset of instability (a) axisymmetric outer mode O-S, with stronger circulations in the outer fluid and (b) axisymmetric inner mode I-S, with stronger circulations in the inner fluid. The vortices depicted in the figure are projections of the streamlines of the flow onto a cross section of the cylindrical channel. A single axial periodic cell is visualized, i.e., $z \in [-\pi/(k_c), \pi/(k_c)]$. The critical parameters are (a) $Re_c = 992.83$, $k_c = 5.167$, $m_c = 0$, $\mu_{12} = 0.525$, $\rho_{12} = 2$, $b = 0.5$, $a = 0.1$ (b) $Re_c = 2353.736$, $k_c = 10.954$, $m_c = 0$, $\mu_{12} = 0.2$, $\rho_{12} = 2$, $b = 0.5$, and $a = 0.1$.

D. Small interface deformation at $O(Ca)$

The results presented in Figures 5 and 6 are the $O(Ca^0)$ approximations to the secondary flows. At this order of approximation, interfacial deformations are entirely absent. However, we can calculate the interfacial deformation at $O(Ca^1)$, from the pressure and velocity fields at $O(Ca^0)$, using the normal stress balance (cf. Sec. IV). The result of this calculation for the case of Figure 5(a) is presented in Figure 7. Here, the pressure perturbations at the interface have been normalized by the value of $\hat{p}_{1,0}$ at $(x = b, z = 0)$. The interface deflection has also been normalized by its magnitude at $(z = 0)$.

In most cases, we find that the pressure forces dominate the viscous normal stresses at the interface (cf. (41)) and are an order of magnitude greater. In Figure 7, the perturbed pressure at $z = 0$ is positive within the inner fluid (Figure 7(a)) and negative in the outer fluid (Figure 7(b)). Thus, the interface is pushed outwards at $z = 0$, as shown in Figure 7(c).

IX. DEPENDENCE OF STABILITY ON THE CURVATURE RATIO (a)

The centrifugal instability sets in when destabilizing centrifugal forces overcome viscous forces. The relative strength of centrifugal forces is directly related to the magnitude of the Reynolds number (Re) and the curvature ratio (a). Hence, in a channel with a smaller curvature ratio
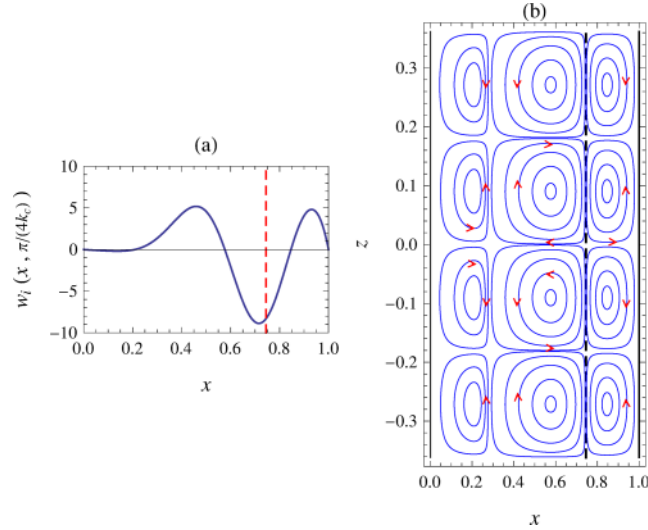
FIG. 6. Secondary circulations at the onset of instability of the second most unstable mode in the case of single-phase flow. Parameters: $Re_c = 593.92$ and $k_c = 8.683$ (for the most unstable mode, $Re_c = 121.35$ and $k_c = 4.087$). This single-phase mode is identical to the uniform mode which is critical in two-phase flow when the fluids have equal viscosities and densities and the interface is located between the two outer vortices.

(less curved), the critical Reynolds number is larger. This relationship is depicted in Figure 8 (solid line).

In the limit of small curvature ratios, the critical Reynolds number is nearly proportional to $a^{-1/2}$. This relationship is exact if the simplified equations used by Dean are adopted[1] (cf. Sec. I of the supplementary material[17]). Under this simplification, a critical Dean number which is independent of a can be defined as $De_c = Re_c\sqrt{a}$. In our results, De_c actually varies slowly with a, since we have retained all terms of the form aRe and ma in the equations. In Figure 8, we have plotted estimates of the critical Reynolds number (red markers) obtained by assuming De_c to be independent of a. Here, De_c is first calculated at $a = 0.01$ (value is 150.302) and then used to estimate the critical Reynolds number at other values of a, as $De_c a^{-1/2}$. The approximation works well for small values of a but becomes increasingly inaccurate as a is increased above 0.1.

In the remainder of this work, we only present results for $a = 0.1$. The critical Reynolds number at other small curvature ratios can be estimated by calculating the critical Dean number.
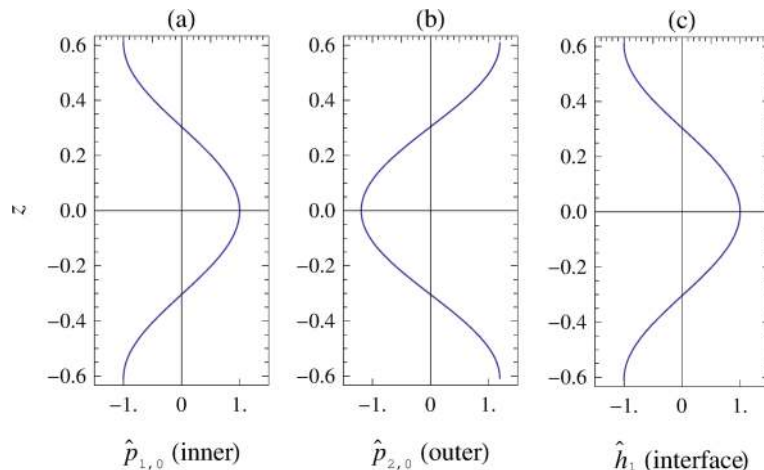

FIG. 7. Pressure perturbations (a) and (b) and interface deflection (c) at $O(Ca^1)$ for same case as Figure 5(a). Parameter values: $Re_c = 992.83$, $k_c = 5.167$, $m_c = 0$, $\mu_{12} = 0.525$, $\rho_{12} = 2$, $b = 0.5$, and $a = 0.1$.
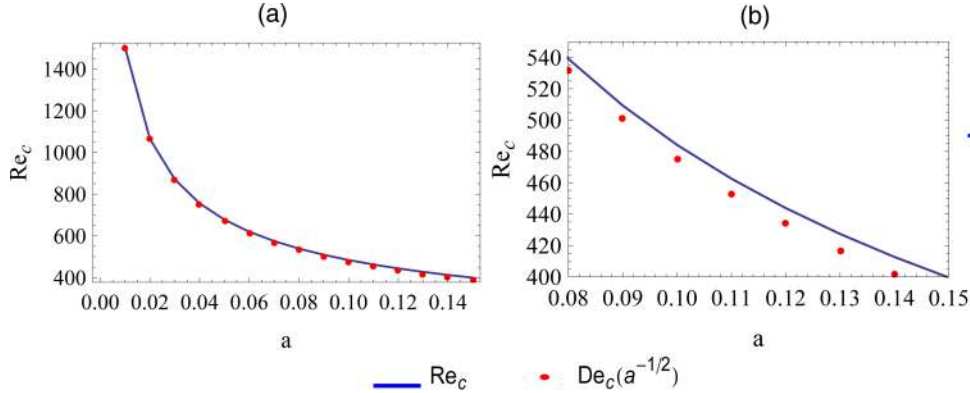
FIG. 8. Variation of Re_c with a for $\mu_{12} = 0.525$, $\rho_{12} = 1$, and $b = 0.5$. Figure (b) is an enlarged version of (a). The solid line represents the computed values of Re_c and the circular markers represent approximate values obtained by keeping the Dean number constant at a value of 150.302 (evaluated for the case of $a = 0.01$). The instability mode is axisymmetric ($m_c = 0$) and k_c is very nearly independent of a with a value of 5.02 ± 0.007.

Next, the effect of a on the critical instability mode is discussed. Variation of the curvature ratio within the range 0.01–0.3 does not affect the nature of the critical mode, i.e., if the critical mode is axisymmetric and stationary ($m_c = 0$) for one value of a, then it remains so for all other values as well. Similarly, while the value of m_c for non-axisymmetric does change with a, it remains bounded away from zero. So varying a cannot cause a transition from a non-axisymmetric critical mode to an axisymmetric one. The influence of a on k_c is small; for all the cases studied in Figure 8, we have $k_c = 5.02 \pm 0.007$.

To understand the effect of increasing curvature ratio on the shape of the spiral modes, the influence of a on the azimuthal wave number of non-axisymmetric modes is investigated. Results for the critical mode at different curvature ratios are presented in Table I for a case of a non-axisymmetric critical mode ($\mu_{12} = 1$, $\rho_{12} = 1$, and $b = 0.72$). The dimensional critical azimuthal *wavelength* equals $\frac{2\pi}{m_c} R^*$, which in non-dimensional terms is $\frac{2\pi}{m_c a}$. In Table I, we observe that ($a m_c$) decreases as a decreases, implying that the azimuthal wavelength of the critical mode increases as the channel becomes straighter, i.e., the spirals will have smaller pitch angles in channels which are less curved.

X. MODE SWITCHING ACROSS PARAMETER SPACE

Six different types of instability modes were identified in Sec. VIII. The critical mode can switch from one type to another as parameters are varied. Such transitions signify a qualitative change (bifurcation) in the secondary flow states. For example, at an O-S to I-S transition, the dominant vortex shifts from the outer to the inner fluid, whereas stationary axisymmetric vortices give way to rotating spirals at an O-S to O-T transition. These transitions are codimension-two bifurcations (since two parameters must be specified: the Reynolds number and another parameter such as the viscosity ratio).

TABLE I. The critical mode (m_c and k_c) and the critical Reynolds number (Re_c) at various values of the curvature ratio (a) for $\mu_{12} = 1$, $\rho_{12} = 1$, and $b = 0.72$.

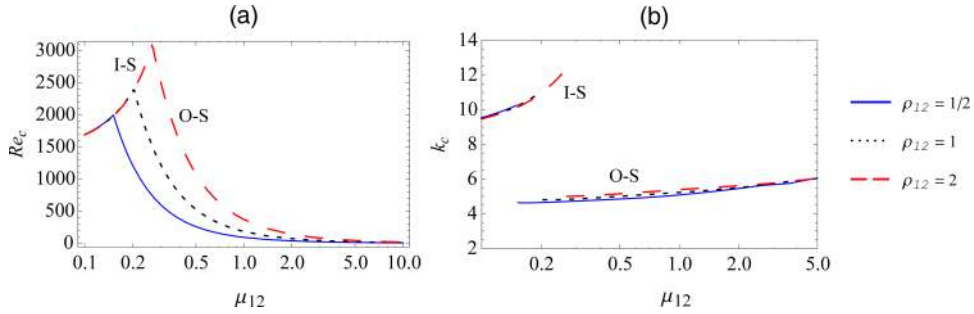| a	m_c	k_c	Re_c
0.1	1.970	9.107	561.211
0.05	2.568	9.039	787.772
0.01	5.207	8.971	1750.670

FIG. 9. Mode switching with variation in viscosity ratio considering different density ratios. The critical mode switches from I-S to O-S as the viscosity ratio is increased, i.e., the stronger vortex moves from the inner to the outer fluid. The critical Reynolds number is plotted in (a) while the critical axial wave number is plotted in (b). The critical azimuthal wave number is $m_c = 0$ (axisymmetric). Parameter values: $b = 0.5$ and $a = 0.1$.

In this section, we analyze the critical instability mode across parameter space, i.e., the density ratio, the viscosity ratio, and the volume fraction (interface location). The goal is to locate various codimension-two bifurcations and identify the physical causes for these transitions.

A. Variation of viscosity and density ratios

First, we analyze the effect of the viscosity ratio. In Figure 9, the critical Reynolds number (Re_c) and the axial wave number (k_c) are plotted as a function of the viscosity ratio for different density ratios. For each density ratio, the profiles of Re_c and k_c consist of two distinct smooth curves which correspond to two different modes, each of which is critical for different ranges of the viscosity ratio. A transition occurs between these modes at the point marked by discontinuity in the case of k_c and non-differentiability in the profile of Re_c.

While both these modes are axisymmetric ($m_c = 0$), they have different internal velocity fields. Examining the corresponding eigenfunctions (as in Figure 5), we find that the critical mode at small μ_{12} is an I-S mode, i.e., the cross flow is much stronger in the inner fluid. At small μ_{12}, the Rayleigh discriminant (cf. Sec. VI) is more negative within the inner fluid, implying stronger destabilizing centrifugal forces therein. In addition, viscous effects are weaker within the inner fluid. Both these factors promote cross flow within the inner fluid. However as μ_{12} is increased, the variation of the Rayleigh discriminant and viscous forces eventually reverse to support stronger circulatory flows within the outer fluid (O-S mode). Hence, increasing μ_{12} stabilizes the I-S mode while simultaneously destabilizing the O-S mode. This leads to a transition between the two modes.

This transition between modes is more easily visualized in Figure 10. Here, the marginal Reynolds number is plotted as a function of the axial wave number for two viscosity ratios on either side of the transition in Figure 9 (dotted curve). Both profiles have two local minima. The one at larger k_c is the I-S mode (smaller vortices, cf. Sec. VIII) and is the global minimum at the lower value of $\mu_{12} = 0.26$. As the viscosity ratio increases, this local minimum rises (I-S mode becomes more stable) while the minimum at small k_c (O-S mode) falls to smaller values of Re_c. Eventually, the global minima switches from one mode to the other (as seen for $\mu_{12} = 0.281$ in Figure 10), marking the transition of the critical mode.

On comparing the results for different density ratios in Figure 9, we find that increasing the density ratio shifts the transition between I-S and O-S modes to higher viscosity ratios. In other words, increasing the relative density of the inner fluid causes the I-S mode to remain critical over a larger range of viscosity ratios, thereby promoting the formation of stronger vortices within the inner fluid. These results indicate that the cross flow at the onset of instability has a tendency to be stronger in the fluid with higher density. This is consistent with the fact that the magnitude of the centrifugal force experienced by a fluid is proportional to its density.

A rather unexpected result is that the I-S mode is unaffected by changes in the density ratio. This is demonstrated by the I-S mode plots in Figure 9(a), which coincide for all three density
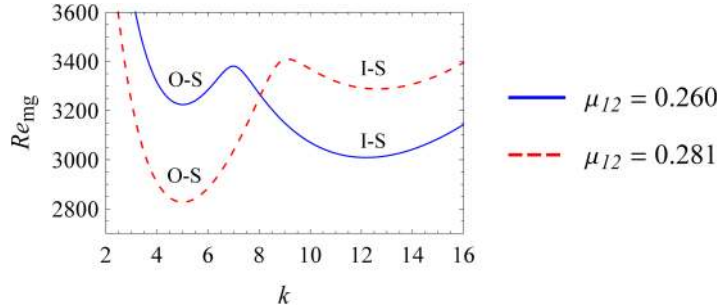
FIG. 10. Plot of the marginal Reynolds number as a function of the axial wave number, in the neighbourhood of the transition in Figure 9 ($m_c = 0$). Parameter values: $m = 0$, $b = 0.5$, $\rho_{12} = 1$, and $a = 0.1$.

ratios. On the other hand, the O-S mode is stabilized as the density of the inner fluid increases (outer fluid decreases). Thus, the mode transition shifts to larger μ_{12} as ρ_{12} is increased.

B. Variation of the volume fraction

Next, we investigate the effect of changes in the relative fluid volumes (variation of the interface location, b) on the critical mode. In this case, the critical mode can switch between stationary and travelling modes. For clarity, we first focus on stationary axisymmetric modes alone and study the transition between O-S, U-S, and I-S modes. Towards this end, we plot the least marginal Reynolds numbers for $m = 0$ as a function of the volume fraction in Figure 11. Here, the most unstable axisymmetric mode switches from O-S to U-S to I-S as the volume fraction occupied by the inner fluid is increased (b is increased). It follows that the cross flow tends to be stronger, at the onset of instability, within the fluid which occupies a larger fraction of the channel. The other fluid occupying a smaller volume fraction is confined in a narrower region and hence, the circulatory flow within it is suppressed.

As the most unstable axisymmetric mode switches from O-S to I-S in Figure 11, it undergoes an intermediate transition to the U-S mode. The U-S mode has a cross flow of comparable intensity in both fluids (cf. Figure 6) and represents a compromise between the opposing natures of the O-S and I-S modes.

The dashed horizontal lines in Figure 11 mark the stability results for the single-phase case. As expected, the single-phase results are obtained when the volume fraction of either fluid approaches unity.

The calculations in Figure 11 are extended to unequal fluid properties in Figure 12. As was the case in Figure 9, the density ratio does not change the results for the I-S mode. Only the U-S and
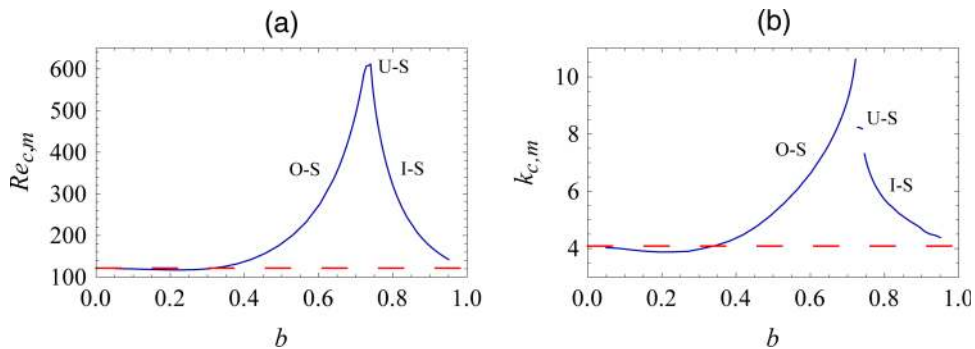

FIG. 11. Mode switching with variation in the interface position, considering only axisymmetric modes. The most unstable axisymmetric mode switches from O-S to U-S to I-S as the interface nears the outer wall. (a) Plot of the least marginal Reynolds number and (b) plot of the least marginal axial wave number for the case of $m = 0$. The dashed (red) line is the value for single-phase flow. Parameter values: $\mu_{12} = 1$, $\rho_{12} = 1$, and $a = 0.1$.
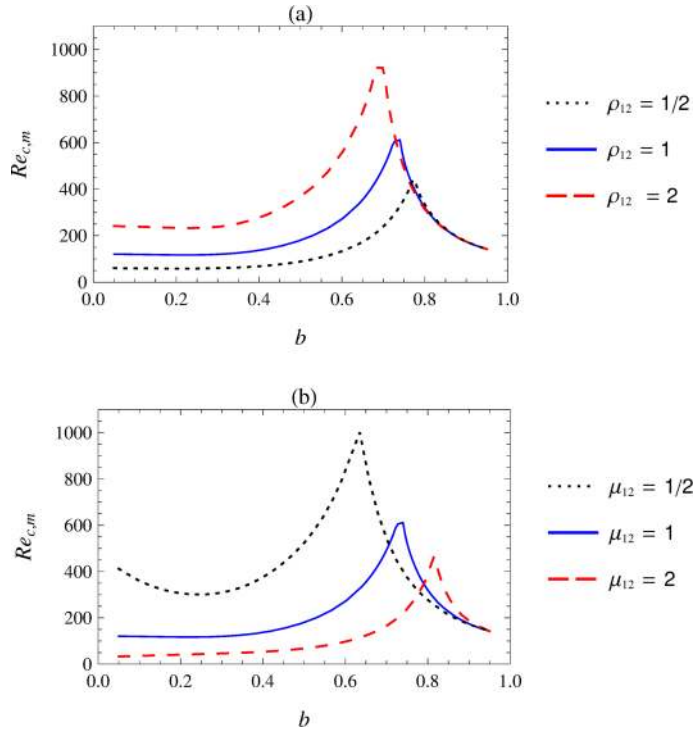
FIG. 12. Effect of density ratio (a) and viscosity ratio (b) on mode switching with variation in the interface position, considering only axisymmetric modes. Parameter values: (a) $\mu_{12} = 1$, $a = 0.1$ (b) $\rho_{12} = 1$ and $a = 0.1$.

O-S results are affected. On the other hand, the viscosity ratio changes the stability results of all three modes. Variation of the fluid properties cause a shift in the point of transition. Larger outer fluid densities cause the O-S mode to be critical over a larger range of volume fractions. A smaller value of the outer fluid's viscosity has the same effect. In summary, *the outer mode is more unstable* (the cross flow at the onset of instability is stronger in the outer fluid) *when the outer fluid has a lower viscosity, higher density, and a larger volume fraction.*

C. Transition to rotating spirals

So far we have discussed transitions between axisymmetric modes. While axisymmetric modes are critical for all the cases in Figure 9, they are not critical for all values of b in Figure 11. The transition to non-axisymmetric rotating spirals ($m_c \neq 0$) is depicted in Figure 13, which plots the least marginal Reynolds number for $m = 0$, 2, and 3, as b is varied. Travelling spiral modes become important in the range of b values corresponding to the transition between the different axisymmetric modes (O-S to I-S via U-S). In this range of volume fractions, the system is relatively stable to axisymmetric disturbances and the non-axisymmetric rotating spirals become critical instead. Figure 13 focuses on this region of interest and depicts the transition of the critical mode from O-S to O-T to U-S to I-T and finally to I-S as b is increased. The four transition points are marked by the intersection of the curves in Figure 13. In this figure, we show results for travelling modes corresponding to relatively small values of m as these are the most unstable. Modes with larger azimuthal wave numbers are stabilized by diffusive effects of viscous momentum transfer and have higher marginal Reynolds numbers.

It should be noted that the switch from an axisymmetric to a non-axisymmetric mode occurs when the minimum of a non-axisymmetric ($m \neq 0$) neutral curve falls below that of the $m = 0$ neutral curve, and vice versa. Here, the location of the critical Reynolds number shifts from one neutral curve to another. In contrast, the switch between different axisymmetric modes (e.g., O-S to I-S) occurs along the same neutral curve, corresponding to $m = 0$. The transition occurs when the
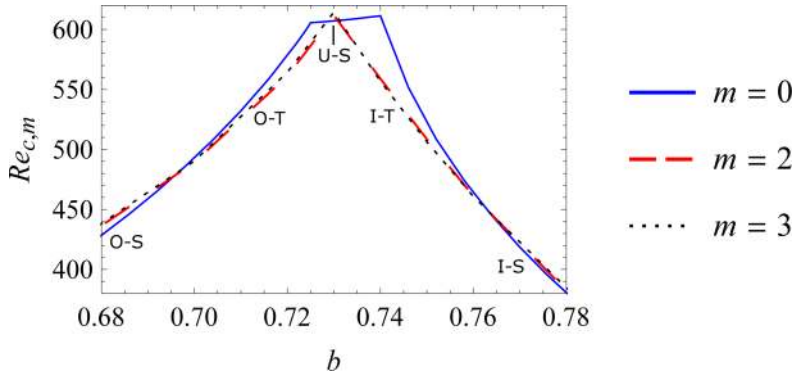
FIG. 13. Mode switching between axisymmetric and non-axisymmetric modes. Plot of the least marginal Reynolds number as a function of the interface position. Parameter values: $\mu_{12} = 1$, $\rho_{12} = 1$, and $a = 0.1$.

global minimum of the neutral curve of $m = 0$ shifts location from one local minimum to another, as demonstrated in Figure 10.

Another illustration of critical mode switching is given in Figure 14, where the variation of the density ratio causes a switch from O-S at low ρ_{12} to O-T, I-T, and I-S as ρ_{12} is increased. The figure is depicted in two parts for the sake of clarity. Again, travelling spiral modes are critical in the region where the axisymmetric modes switch from O-S to I-S. For density ratios from 0.6 to 1, the mode with $m_c = 3$ is critical. The corresponding critical frequency Im$[\omega]$ which is related to the speed of the rotating spiral by $(-\text{Im}[\omega] \, (k_c^2 + m_c^2)^{-1/2})$ is plotted in Figure 15. The azimuthal motion of the spiral waves is in the direction of the flow (because Im$[\omega] < 0$).

In Figure 13, we find that the U-S mode is critical over a very small range of interface positions, while in Figure 14 it is never critical. This is typical of the U-S axisymmetric mode and in an experiment, one is much more likely to observe either O-S/I-S axisymmetric vortices or non-axisymmetric rotating spirals.

A common feature, underlying all the results in this section, is that the outer fluid is more susceptible to the centrifugal instability. This is particularly evident in Figures 9 and 11. In Figure 9, the mode transition does not occur at a viscosity ratio of unity, despite both fluids having equal densities and occupying equal volumes of the channel ($b = 0.5$ and $\rho_{12} = 1$). Instead, the transition occurs at a low viscosity ratio. Moreover, when the viscosities are equal, the O-S mode is critical and the outer fluid dominates the secondary flow. Similarly, in Figure 11, the transition from O-S to I-S occurs only when the inner fluid occupies significantly more than half the channel. Clearly, the
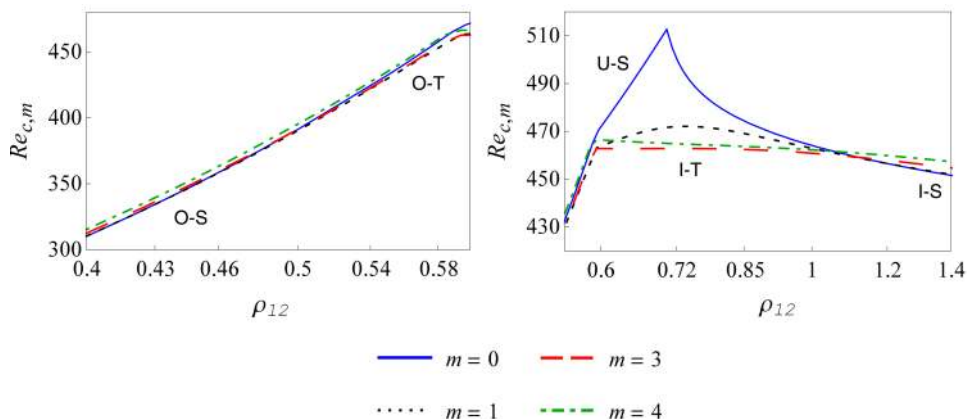

FIG. 14. Mode switching with variation in density ratio. Plot of the least marginal Reynolds number as a function of the density ratio. The figure is split into two parts for better clarity. Parameter values: $\mu_{12} = 1$, $b = 0.76$, and $a = 0.1$.
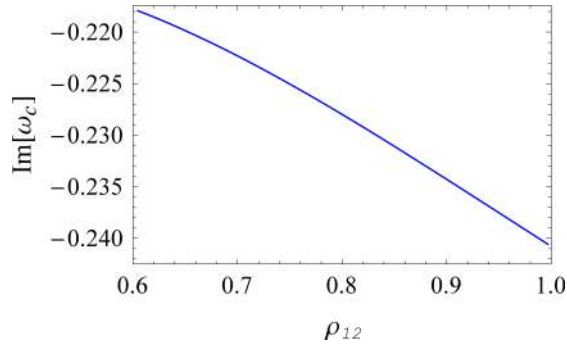
FIG. 15. Critical frequency $Im[\omega]$ which corresponds to the critical mode $m_c = 3$ in Figure 14.

outer mode (with stronger circulations in the outer fluid) is preferred by the system. This bias occurs because the stratification of angular momentum is more unstable in the outer fluid, as reflected by the negative values of the Rayleigh discriminant (cf. Sec. VI). This feature of the two-phase centrifugal instability leads us to investigate the influence of the arrangement of fluids on stability. This is the subject of Sec. XI.

XI. EFFECT OF FLUID ARRANGEMENT ON STABILITY

Based on the results in Secs. VI and X, we expect the arrangement of fluids to have a significant influence on stability. As an example, consider two fluids of nearly equal densities and volume fractions, but with viscosities in the ratio 1:6. If the less viscous fluid is taken as the outer fluid, then $\mu_{12} = 6$, else $\mu_{12} = 1/6$. The Rayleigh discriminant profile for these two cases is very different, as shown in Figure 2. Figure 9 shows that if the less viscous fluid is placed on the outer side ($\mu_{12} = 6$), then the O-S mode will be critical, else the I-S mode will be critical.

Apart from the nature of the critical mode, the critical pressure drop G_c^* will also depend on the arrangement of fluids. G_c^* is the minimum magnitude of the pressure gradient required for the flow to become unstable. We can determine the more unstable fluid arrangement by identifying the arrangement that requires a smaller critical pressure drop.

If the two configurations are labelled A and B, then in the framework of our mathematical model, we obtain two stability problems with parameter sets $(\rho_{12})_A$, $(\mu_{12})_A$, $(b)_A$ and $(\rho_{12})_B$, $(\mu_{12})_B$, $(b)_B$, respectively. Since configurations A and B are related by interchanging the locations of the fluids, the following relations hold between the two sets of parameters,

$$(\mu_{12})_B = \frac{1}{(\mu_{12})_A}; \quad (\rho_{12})_B = \frac{1}{(\rho_{12})_A}; \quad (b)_B = 1 - (b)_A. \tag{56}$$

The corresponding critical Reynolds number is $(Re_c)_A$ and $(Re_c)_B$, from which the ratio of critical pressure drops may be obtained using (9),

$$\frac{(G_c^*)_A}{(G_c^*)_B} = \frac{(Re_c)_A}{(Re_c)_B} \frac{(\mu_{12})_A}{(\rho_{12})_A}. \tag{57}$$

From Eq. (57), we see that the ratio of critical Reynolds numbers cannot be used to compare the two configurations. This is because the value of the Reynolds number depends on the density and viscosity scales. If the fluids have different physical properties ($\rho_{12} \neq 1$, $\mu_{12} \neq 1$), then the ratio of critical Reynolds numbers will not be unity when configurations A and B are equally unstable, with $(G_c^*)_A = (G_c^*)_B$. Thus, we must compare the critical pressure drops in order to reliably identify the more unstable fluid arrangement.

Now, we study a few specific fluid pairs with the aim of developing general rules for identifying the more unstable configuration. First, consider the case of the interface located at $b = 0.5$, with fluids of equal densities but unequal viscosities. Let A (B) be the configuration with the more viscous fluid on the inner (outer) side of the channel. In Figure 16, the ratio of critical pressure
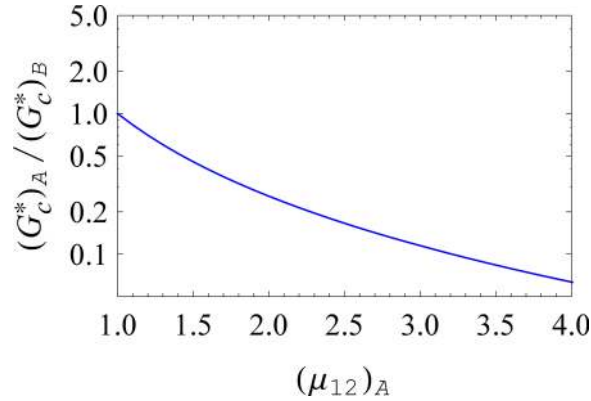
FIG. 16. Plot of the ratio of critical pressure drops for configurations A and B as the viscosity ratio is varied. A: more viscous fluid on the inner side of the channel. B: more viscous fluid on the outer side. Placing the less viscous fluid on the outer side is destabilizing. Parameter values: $\rho_{12} = 1$, $b = 0.5$, and $a = 0.1$.

drops is plotted as a function of the viscosity ratio (as defined for configuration A). Here, $(G_c^*)_A$ is always less than $(G_c^*)_B$, i.e., the configuration with the less viscous fluid on the outer side is more unstable. The difference in the stability of the two configurations increases with the difference in the viscosities of the two fluids. A similar result was obtained by Renardy and Joseph for two-phase Taylor Couette flow.[4]

Next, we consider two fluids of equal viscosity but unequal densities, with the interface at $b = 0.5$. A (B) is the configuration in which the denser fluid is on the inner (outer) side of the channel. The ratio of critical pressure drops is plotted for various density ratios (as defined in A) in Figure 17. In this case, $(G_c^*)_A$ is always greater than $(G_c^*)_B$ indicating that the configuration with the denser fluid on the outer side is more unstable. Interestingly, while this arrangement destabilizes the centrifugal instability, it stabilizes the Rayleigh-Taylor and viscosity-induced instabilities.[13]

From Figures 16 and 17, we see that the viscosity and density of the outer fluid have opposing effects on stability. Ideally, the outer fluid should be more dense, as well as less viscous, to promote instability. This need not be the case in practice; Figure 18 depicts results for a situation in which the fluid with a greater density has twice the viscosity of the less dense fluid. A is the configuration in which the more dense, more viscous fluid is located on the inner side of the channel. On the basis of Figures 17 and 16, the density difference is expected to stabilize A while the viscosity difference destabilizes A. The ratio of critical pressure drops, plotted in Figure 18, shows that the viscous effect dominates when the density difference between the two fluids is small while the density effect becomes prominent at larger density ratios. These two effects balance out at a density
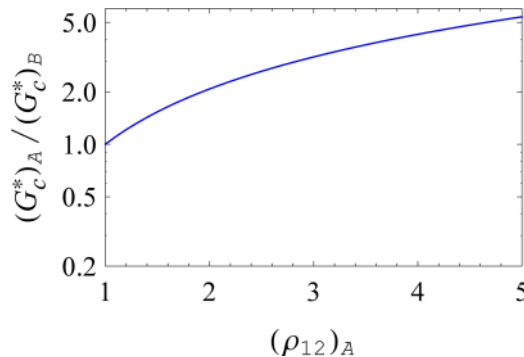

FIG. 17. Plot of the ratio of critical pressure drops for configurations A and B as the density ratio is varied. A: more dense fluid on the inner side of the channel. B: more dense fluid on the outer side. Placing the denser fluid on the outer side stabilizes the centrifugal mode. Parameter values: $\mu_{12} = 1$, $b = 0.5$, and $a = 0.1$.
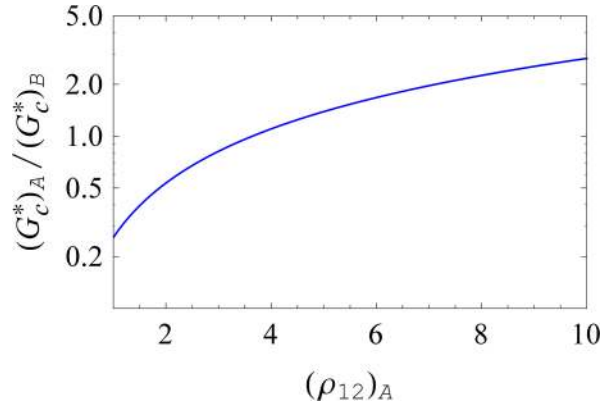
FIG. 18. Plot of the ratio of critical pressure drops for configurations A and B as the density ratio is varied. The denser fluid has twice the viscosity of the less dense fluid. A: more dense, more viscous fluid on the inner side of the channel. B: more dense, more viscous fluid on the outer side. Parameter values: $(\mu_{12})_A = 2$, $b = 0.5$, and $a = 0.1$.

ratio of approximately 3.7:1 when $(G_c^*)_A = (G_c^*)_B$ (A and B are equally unstable). Considering that the viscosity ratio is only 2:1, it seems that *viscosity differences have a greater impact on the centrifugal instability than equivalent density differences.*

Finally, we consider two fluids with equal physical properties but occupying unequal volume fractions of the channel. In this case, the ratio of critical pressure drops equals the ratio of critical Reynolds numbers, because $\rho_{12} = \mu_{12} = 1$ in (57). The critical Reynolds number was plotted as a function of the volume fraction in Figure 11(a). From this figure, we see that the critical Reynolds number is lower when $b < 0.5$. Thus, the critical pressure drop is lower when the volume fraction of the inner fluid is smaller. Hence, the flow will be more unstable when the fluid which occupies a larger fraction of the channel is located on the outer side.

The cases studied in this section lead to the following general principle: *the two-phase flow is rendered more unstable, to the centrifugal instability, when the fluid which is less viscous, more dense, and has a larger volume fraction is chosen as the outer fluid.* Interestingly, these criteria also ensure that the critical mode will be an outer mode (O-S or O-T) with a stronger cross flow within the outer fluid (cf. Sec. X). It is quite possible that the pair of fluids will have properties with opposing effects on the system's stability (cf. Figure 18). For example, the denser fluid could have a larger viscosity and occupy a smaller volume fraction of the channel. In such cases, the more unstable configuration is not obvious but can be determined by applying the methodology described in this section.

XII. CONCLUDING REMARKS

We have studied the centrifugal instability of two-phase stratified Poiseuille flow in a curved channel. This problem is a two-phase analogue of the classic Dean problem[2] wherein pressure driven flow is susceptible to an instability due to unstable stratification of angular momentum. In the general two-phase problem, the flow can also become unstable to interfacial modes in addition to the centrifugal mode. These include the viscosity-induced instability, Rayleigh-Taylor, and capillary breakup. In this work, we have analyzed the regime of small capillary numbers, wherein interfacial deformations are suppressed by surface tension. (The capillary instability is excluded because of the relatively large radius of curvature of the channel.) Under these circumstances, the centrifugal mode dominates, allowing us to study its features in detail. The results presented here for the two-phase centrifugal instability, when taken in conjunction with previous work on interfacial modes,[14,25,13,11,10] provide a foundation for a general stability analysis of stratified flow in curved channels.

Studies across parameter space revealed six types of critical centrifugal modes—three axisymmetric (I-S, U-S, and O-S) and three non-axisymmetric (I-T, U-T, and O-T). The axisymmetric

modes are critical over most of the parameter space. They correspond to a stationary (S) secondary flow consisting of axisymmetric toroidal vortices within each fluid. The non-axisymmetric modes correspond to travelling (T) waves of rotating spiral vortices. The circulatory flow can be stronger within one of the fluids or of comparable intensity in both, leading to a further classification into inner modes (I), outer modes (O), and uniform modes (U). A stronger circulatory flow tends to arise in the fluid with either a lower viscosity, a higher density, or a larger volume fraction.

This rich variety of instability modes is a characteristic of the two-phase system that is not seen in the single-phase case. This is due to the influence of the viscosities and interface position on the stratification of angular momentum in the base state, as quantified by the Rayleigh discriminant (Sec. VI). In addition, all physical parameters influence the interplay between inertial and viscous forces which governs the growth of the instability.

It is important to note that even for small super-critical Reynolds numbers, a range of both axisymmetric modes and travelling waves can become unstable. This is because the marginal Reynolds numbers of these modes are closely spaced, as shown in Figure 3. This is especially true for parameters close to mode switching points (codimension-two bifurcations). The interaction between different modes can result in a variety of flow patterns. A similar situation exists in the single-phase Taylor-Couette flow near the transition from Taylor vortex flow (axisymmetric mode) to spiral flow (non-axisymmetric travelling wave).[31,32] Interaction between modes results in flow patterns such as ribbons, wavy vortices, twisted vortices, and modulated periodic flows.[33,29,34] These flows have been observed experimentally[31] in single-phase Taylor-Couette flow and explained by group theoretic methods (equivariant bifurcation theory).[27,33,29] In the two-phase flow studied here, an even richer variety of patterns may be expected due to the inter-fluid interaction across the interface.

The stability of the flow was found to depend on the arrangement of the fluids. We demonstrated that the critical Reynolds number cannot be used to compare different fluid arrangements. Instead, we compared the minimum pressure drop required for the onset of instability and found a general rule: *the flow is more unstable when the fluid with a higher density, lower viscosity*, *and larger fractional flow area is taken as the outer fluid*. (These are the same conditions that promote stronger circulations in the outer fluid.) These results will be useful in designing liquid-liquid mass transfer devices which use vortex motion to enhance interphase mass transfer. Such a device based on two-phase Taylor-Couette flow has been studied recently.[7] Our results support the viability of a similar system based on pressure driven flow. These devices require the fluids to remain stratified. In view of this, the dependence of the centrifugal instability on the fluid configuration is quite favorable. Placing the denser fluid on the outer side of the channel not only stabilizes the interface to the Rayleigh-Taylor instability (stable light over heavy configuration) but also promotes vortex formation by inducing the centrifugal instability at lower pressure drops.

The two-phase eigen value problem, associated with the linear stability analysis, has been solved by a Galerkin spectral method which utilizes a novel basis of recombined Chebyshev functions—two phase RCGS method. This recombined basis satisfies the boundary conditions analytically. Thus, boundary conditions do not have to be included separately in the matrix eigen value problem, as is conventionally done in standard Tau and collocation spectral methods.[35] In these traditional techniques, the rows corresponding to boundary conditions often cause the QZ algorithm to generate spurious, unbounded eigenvalues. This difficulty is circumvented by the RCGS method. Another advantage of this method is the smaller size of the matrix for the same number of spectral modes. This method is a two-phase extension of the technique used by Gelfgat and coworkers[20–22] and can be applied to other two-phase problems which have boundaries located along co-ordinate surfaces. The information given in the supplementary material[17] will aid in such applications.

ACKNOWLEDGMENTS

[1] W. R. Dean, "Fluid motion in a curved channel," Proc. R. Soc. A **121**, 402 (1928).

[2] P. G. Drazin and W. H. Reid, *Hydrodynamic Stability*, 2nd ed. (Cambridge University Press, New York, 2004).

[3] E. M. Sparrow, "On the onset of flow instability in a curved channel of arbitrary height," ZAMP **15**, 638 (1964).

[4] Y. Renardy and D. D. Joseph, "Couette flow of two fluids between concentric cylinders," J. Fluid Mech. **150**, 381 (2006).

[5] G. Baier and M. D. Graham, "Two-fluid Taylor–Couette flow: Experiments and linear theory for immiscible liquids between corotating cylinders," Phys. Fluids **10**, 3045 (1998).

[6] G. Baier and M. D. Graham, "Two-fluid Taylor-Couette flow with countercurrent axial flow: Linear theory for immiscible liquids between corotating cylinders," Phys. Fluids **12**, 294 (2000).

[7] G. Baier, M. D. Graham, and E. N. Lightfoot, "Mass transport in a novel two-fluid Taylor vortex extractor," AIChE J. **46**, 2395 (2000).

[8] J. Peng and K.-Q. Zhu, "Linear instability of two-fluid Taylor–Couette flow in the presence of surfactant," J. Fluid Mech. **651**, 357 (2010).

[9] A. Y. Gelfgat, A. L. Yarin, and P. Z. Bar-Yoseph, "Three-dimensional instability of a two-layer Dean flow," Phys. Fluids **13**, 3185 (2001).

[10] S. Chandrasekhar, *Hydrodynamic and Hydromagnetic Stability* (Dover, New York, 1981).

[11] L. E. Johns and R. Narayanan, *Interfacial Instability* (Springer-Verlag, New York, 2002).

[12] C.-S. Yih, "Instability due to viscosity stratification," J. Fluid Mech. **27**, 337 (1967).

[13] P. A. M. Boomkamp and R. H. M. Miesen, "Classification of instabilities in parallel two-phase flow," Int. J. Multiphase Flow **22**, 67 (1997).

[14] S. G. Yiantsios and B. G. Higgins, "Linear stability of plane Poiseuille flow of two superposed fluids," Phys. Fluids **31**, 3225 (1988).

[15] R. D. Gibson and A. E. Cook, "The stability of curved channel flow," Q. J. Mech. Appl. Math. **27**, 149 (1974).

[16] W. H. Reid, "On the stability of viscous flow in a curved channel," Proc. R. Soc. A **244**, 186 (1958).

[17] See supplementary material at http://dx.doi.org/10.1063/1.4921631 which describes the gentle curvature approximation and the recombined Galerkin spectral method. Convergence of the spectral method is demonstrated and its results are verified with a shooting technique.

[18] L. G. Leal, *Advanced Transport Phenomena-Fluid Mechanics and Convective Transport Processes* (Cambridge University Press, New York, 2007).

[19] M. Cross and H. Greenside, *Pattern Formation and Dynamics in Nonequilibrium Systems* (Cambridge University Press, New York, 2009).

[20] A. Y. Gelfgat and I. Tanasawa, "Numerical analysis of oscillatory instability of buoyancy convection with the Galerkin spectral method," Numer. Heat Transfer, Part A **25**, 627 (1994).

[21] A. Y. Gelfgat, P. Z. Bar-Yoseph, and A. L. Yarin, "Stability of multiple steady states of convection in laterally heated cavities," J. Fluid Mech. **388**, 315 (1999).

[22] A. Y. Gelfgat, "Two and three dimensional instabilities of confined flows: Numerical study by a global Galerkin method," Comput. Fluid Dyn. J. **9**, 437 (2001).

[23] S. D. Conte, "The numerical solution of linear boundary value problems," SIAM Rev. **8**, 309 (1966).

[24] P. J. Schmid and D. S. Henningson, *Stability and Transition in Shear Flows* (Springer-Verlag, New York, 2001), pp. 479–483.

[25] A. P. Hooper, "The stability of two superposed viscous fluids in a channel," Phys. Fluids **1**, 1133 (1989).

[26] M. C. Cross and P. C. Hohenberg, "Pattern formation outside of equilibrium," Rev. Mod. Phys. **65**, 851 (1993).

[27] J. D. Crawford and E. Knobloch, "Symmetry and symmetry-breaking bifurcations in fluid dynamics," Annu. Rev. Fluid Mech. **23**, 341 (1991).

[28] I. Stewart and M. Golubitsky, *Fearful Symmetry: Is God a Geometer?* (Blackwell Publishers, Oxford, 1992).

[29] M. Golubitsky and W. F. Langford, "Pattern formation and bistability in flow between counterrotating cylinders," Physica D **32**, 362 (1988).

[30] R. Tagg, W. S. Edwards, H. L. Swinney, and P. S. Marcus, "Nonlinear standing waves in Couette-Taylor flow," Phys. Rev. A **39**, 3734 (1989).

[31] C. D. Andereck, S. S. Liu, and H. L. Swinney, "Flow regimes in a circular Couette system with independently rotating cylinders," J. Fluid Mech. **164**, 155 (1986).

[32] W. F. Langford, R. Tagg, E. J. Kostelich, H. L. Swinney, and M. Golubitsky, "Primary instabilities and bicriticality in flow between counterrotating cylinders," Phys. Fluids **31**, 776 (1988).

[33] M. Golubitsky and I. Stewart, "Symmetry and stability in Taylor-Couette flow," SIAM J. Math. Anal. **17**, 249 (1986).

[34] N. Itoh, "Development of spiral and wavy vortices in circular Couette flow," Fluid Dyn. Res. **17**, 87 (1996).

[35] J. P. Boyd, *Chebyshev and Fourier Spectral Methods*, 2nd ed. (Dover, New York, 2001).